ELECTRICAL AND OPTICAL CHARACTERIZATION OF GaAs NANOWIRE ARRAYS

ELECTRICAL AND OPTICAL CHARACTERIZATION OF GaAs NANOWIRE ARRAYS

BY

JUNPENG ZHANG, B.Sc. (Hons.), B.Eng

A THESIS

SUBMITTED TO THE SCHOOL OF GRADUATE STUDIES OF MCMASTER UNIVERSITY

IN PARTIAL FULFILLMENT OF THE REQUIREMENTS FOR THE DEGREE OF MASTER OF APPLIED SCIENCE

© Copyright by Junpeng Zhang, August 2014

All Rights Reserved

Master of Applied Science (2014) **McMaster University**

(Department of Engineering Physics) **Hamilton, Ontario, Canada**

TITLE: ELECTRICAL AND OPTICAL CHARACTERIZATION OF GaAs NANOWIRE ARRAYS

AUTHOR: Junpeng Zhang

B. Sc. (Hons.) (Wilfrid Laurier University, Waterloo, Canada)

B. Eng (Jiangsu University, Zhenjiang, China)

SUPERVISOR: Dr. R. R. LaPierre

NUMBER OF PAGES: x, 73

Abstract

III-V semiconductor nanowires (NWs) are often referred to as one-dimensional (1-D) materials because of their high aspect ratios and excellent quantum confinement properties. Spacing between NWs in a NW array is on the order of ~10^2 nm, which is close to the wavelength of visible light. These properties make NWs have excellent light trapping effects and suitability for optoelectronic applications, such as solar cells and photodetectors.

Gallium arsenide (GaAs) has high electron mobility and a band gap of 1.424 eV, which makes it an ideal material for solar cells. Since GaAs NWs can be grown on either GaAs substrates or foreign substrates such as silicon (Si) substrates without lattice mismatch issues, they are being widely studied for photovoltaic applications.

GaAs NWs could be achieved by the vapor-liquid-solid (VLS) method in molecular beam epitaxy (MBE), or etching a GaAs substrate by inductively coupled plasma reactive ion etching (ICP-RIE). Cyclotene was used as the filling material in gaps between NWs to support a low sheet resistance front contact and prevent shunts. An In/ITO contact was developed to achieve a lower contact resistance to n-GaAs NWs than an ITO contact, while it had a similar transmittance as ITO.

A crack test also showed that insertion of a thin indium layer between ITO and GaAs NWs solved the ITO crack issue during heating that resulted from a large difference in coefficients of thermal expansion (CTE) between ITO and cyclotene. Energy dispersive x-ray spectrometry (EDS) was used to determine indium diffusion into NWs, and it showed that indium diffusion was not so significant to damage the features in NWs.

A novel method to achieve substrate-free NW arrays by combining ICP-RIE and selective chemical etching together was also introduced. This method made it possible to measure the transmittance of NW arrays and contact layers for the first time. Absorption of GaAs NW arrays with various NW diameters and periods were also determined experimentally.

Acknowledgements

First of all, I would like to express my gratitude to my supervisor Dr. Ray LaPierre, who provided guidance throughout my research and made the completion of this thesis possible. From showing me the blue picture on the first day I started, he has been a tremendous mentor for me for the next two years. I am very grateful for his patience in answering my numerous questions, solving all kinds of problems I encountered, and discussing complex results I have obtained. I have learned a lot from him about how to troubleshoot problems and solve them systematically, and how to make plans for future work. I would also thank other members in "Team LaPierre" for offering me so much help. I would most like to thank Andrew Chia for his assistance on planning experiments and data analysis. Without his help, publishing my first paper would not have been possible. Thanks also go to Jonathan Boulanger for assistance in FIB and TEM analysis, and Paul for maintenance works on the sputtering system. I also appreciate Chris Haapamaki and Sandra Gibson's willingness to discuss sample processing techniques with me.

Next, I would like to thank the technical staff at the Centre for Emerging Device Technologies (CEDT) for keeping all equipment running properly. Shahram Tavakoli's work on MBE growth was the basis of my research. Thanks to Zhiling Peng and Doris Stevanovic's work on keeping the cleanroom running and training me on the equipment, I had a satisfying experience in all sample processing. I would also like to extend my

thanks to Chris Butcher and Julia Huang at the Canadian Centre for Electron Microscopy (CCEM). As SEM and high resolution light microscopy (LM) played an important role in checking sample status and in sample analysis in my research, Chris's kind assistance on operation and training on microscopes were very valuable. I would also like to thank Julia Huang for her proficient operation of FIB on my samples. Special thanks go to Gary Good at Surface Science Western for performing SIMS measurements and having helpful discussions on SIMS analysis. I would also like to acknowledge the administrative staff at the Department of Engineering Physics and the CEDT, especially Marilyn, Alexa and Linda. Finally, I would like to thank my family and friends for constantly supporting me and sharing those unforgettable moments with me. To my mom and dad, thank you for all your support and encouragement on me in pursuing education on the other side of the Earth. I also appreciate your understanding and generosity to your only kid not being able to go home once for the past two years. My special thanks go to Linjing for bringing so many happy moments to my life and making my graduate school experience more joyful. Without your companionship and unwavering support, I would not have known what kind of man I want to be.

Table of Contents

Abstract i
Acknowledgements iii
Table of Contents v
List of Figures vii
List of Tables x
1 Introduction 1
1.1 GaAs Nanowire Fabrication 1
1.2 Application of GaAs Nanowires 5
1.3 Motivation of Present Work 7
1.4 Introduction of Ohmic Contact 9
1.5 Introduction of Indium Tin Oxide (ITO) 12
2 Experiment 15
2.1 Electron Microscopy 15
2.1.1 Scanning Electron Microscopy (SEM) 15
2.1.2 Transmission electron microscopy (TEM) 17
2.2 Secondary Ion Mass Spectrometry (SIMS) 18
2.3 Inductively Coupled Plasma Reactive Ion Etching (ICP-RIE) 19
2.4 Electrical characterization 20
2.5 Optical characterization 21
3 Low Resistance Indium Tin Oxide (ITO) Contact to n-GaAs Nanowires 23
3.1 Introduction 23
3.2 Experimental Details 25
3.3 Results and Discussion 28
3.3.1 Contact Resistance 28

3.3.2 Transmittance 33
3.4 Sheet resistance 34
3.5 Contact pad crack test 35
3.6 Improved Contact Resistance on Etched NWs 37
3.7 Contact Test on Planar GaAs Solar Cells 39
4 Contact Diffusion Test 43
4.1 Introduction 43
4.2 Experimental Details 43
4.3 Results and Discussion 46
5 Transmittance and Reflectance of Nanowire Arrays and Thin Film 50
5.1 Introduction 50
5.2 Experimental Details 51
5.2.1 GaAs Substrate Etching 52
5.2.2 Reflectance and Transmittance Measurement 57
5.3 Results and Discussion 59
5.4 Conclusion 65
6 Conclusions and Future Work 66
6.1 Thesis Summary 66
6.2 Future Work 67
Reference 69

List of Figures

Figure 1.1. VLS mechanism for NW growth: a) a thin Au layer is firstly deposited on the GaAs substrate; b) the substrate is then transferred to an MBE system and heated to form Au droplets; c) Au droplets absorb growth species supplied in the vapor phase and grow GaAs crystals underneath. 2

Figure 1.2. Top-down approach of obtaining NW arrays: a) a GaAs substrate is spin-coated with e-beam resist; b) the substrate is patterned with EBL and developed to remove resist exposed to the electron beam; c) a metal layer is deposited on the substrate; d) residual resist is removed; e) the substrate is etched with ICP-RIE to obtain NWs; f) the metal mask is removed with chemical etching. 4

Figure 1.3. Schematic of band diagram at the metal/n-type semiconductor interface; and carrier transport mechanisms: thermionic emission (TE), thermionic field emission (TFE) and field emission (FE) from semiconductor side to metal side...................................... 12

Figure 2.1. Schematic of sheet resistance measurement by four-point probe technique.. 21

Figure 3.1. SEM images and structure schematics of NWs in Sample A and Sample B. 26

Figure 3.2. (a) Schematic of the different two-point probe configurations used for I-V measurements; (b) J-V' curves of different contacts on sample A; (c) J-V' curves of different contacts on sample B. The probe colors in (a) correspond to the curve colors in (b)... 31

Figure 3.3. (a) Theoretical I-V curves for a photovoltaic device with various specific contact resistances, r_c. (b) Cell efficiency versus r_c extracted from the I-V curves in (a). 32

Figure 3.4. Optical transmittance spectrum of ITO and In/ITO films normalized to the glass slide transmission. The inset shows the unannealed (top) and annealed (bottom) In/ITO film on a glass slide, in comparison with a glass slide without deposition. 34

Figure 3.5. SEM image of cracks on ITO contact pad after annealing. 36

Figure 3.6. J-V' curves of In/ITO contacts on GaAs nanowires with D=100 nm, P=350 nm; D=180 nm, P=350 nm; and D=300 nm, P=700nm. 38

Figure 3.7. (a) Schematic and (b) light microscope image of planar GaAs solar cells contacted by ITO (or In/ITO) pad and Ni/Ge/Au fingers. 40

Figure 3.8. J-V' plots of planar GaAs solar cells contacted with Ni/Ge/Au, In/ITO, and ITO contacts under AM1.5G illumination. 42

Figure 4.1. a) Initial stage and b) final stage of sample preparation for TEM with FIB. . 45

Figure 4.2. EDS line scan a) along NW; b) across the contact/cyclotene interface; c) across the NW at a depth of 50nm; and d) 100 nm under contact layer. 48

Figure 4.3. STEM image of NW/contact interface. Inserted 2D line plot shows the atomic percentage of Ga (green), As (red) and In (blue) at each scan spot in the EDS point-scan. 49

Figure 5.1. Schematic of a) a thin film GaAs solar cell structure grown by MBE; b) GaAs NW solar cell structure after etching with ICP-RIE; c) SEM image of an etched NW array (NW diameter =150nm, pitch = 530nm). 53

Figure 5.2. a) Schematic of sample structure; light microscope image of b) sample front surface; and c) sample back surface after bonding and PL. 55

Figure 5.3. Etching rate and etching depth versus etching time. 56

Figure 5.4. Light microscope images of NW pads after etching in a) reflection mode; and b) transmission mode. 57

Figure 5.5. Experimental setup for (a) reflectance measurement; and (b) transmission measurement for NW pads.. 59

Figure 5.6. Transmittance of off-pad area and twelve nanowire arrays with various diameter D and period P. (a) Each subplot shows NW arrays with the same P ((i): P=460 nm; (ii): P=350 nm; (iii): P=270 nm), but different D (D=110 nm; D=150 nm; D=180 nm; D=225 nm); (b) Each subplot shows NW arrays with the same D((i): D=110 nm; (ii): D=150 nm; (iii): D=180 nm; (iv): D=225 nm), but different P (P=460 nm; P=350 nm; P=270 nm)... 61

Figure 5.7. SEM image of as-etched NW array D1 showing that the metal mask did not get lifted-off. 62

Figure 5.8. Reflectance of off-pad area and twelve nanowire arrays with various D and P. (a) Each subplot shows NW arrays with the same P ((i): P=460 nm; (ii): P=350 nm; (iii): P=270 nm), but different D (D=110 nm; D=150 nm; D=180 nm; D=225 nm)................ 63

Figure 5.9. Absorptance (1-R-T) of off-pad area and twelve nanowire arrays with various D and P. (a) Each subplot shows NW arrays with the same P ((i): P=460 nm; (ii): P=350 nm; (iii): P=270 nm), but different D (D=110 nm; D=150 nm; D=180 nm; D=225 nm). 64

List of Tables

Table 1.1. Summary of GaAs NW array solar cell performance. 7

Table 3.1. Specific contact resistances for different contact materials on samples A and B. 31

Table 3.2. Sheet resistance of ITO film and In/ITO film on glass slide. 35

Table 3.3. Coefficient of thermal expansion (CTE) of several materials at room temperature. 36

Table 3.4. Crack test results of various sizes of ITO (250nm) and In/ITO (25/250nm) square contact pads. 36

Table 3.5. Specific contact resistance of In/ITO contacts on GaAs nanowires with D=100 nm, P=350 nm; D=180 nm, P=350 nm; and D=300 nm, P=700nm. 38

Table 3.6. Thin film GaAs solar cell structure... 39

Table 5.1. Diameters and pitches of NWs in different pads in sample S5. 54

Table 5.2. Average absorptance of NW pads over 400 nm to 900 nm wavelength range.64

1 Introduction

1.1 GaAs Nanowire Fabrication

GaAs nanowire fabrication methods can be divided into two categories based on their formation: bottom-up approach and top-down approach. In the bottom-up approach, GaAs nanowires can be grown by the vapor-liquid-solid (VLS) growth mechanism [1–4], vapor-solid-solid (VSS) growth mechanism [5] and solution-liquid-solid (SLS) growth mechanism [6]. Nanowires obtained by bottom-up growth can achieve high crystal quality and core-shell structures [7]. In addition, nanowires can also be grown in the bottom-up approach on foreign substrates, such as silicon substrates, without lattice mismatch issues [8,9]. The top-down approach is a combination of lithography and etching techniques. After patterning, nanowires can be achieved by either anisotropic chemical wet etching [10] or dry etching [11]. Controlling nanowire diameters, lengths and space between nanowires are relatively easy in the top-down approach [10,11], while they are difficult to achieve in the bottom-up approach. Nanowires with heterostructures could also be achieved in the top-down approach and while retaining material properties. In this thesis, nanowire formation by VLS growth with molecular beam epitaxy (MBE) and by dry etching with inductively coupled plasma reactive ion etching (ICP-RIE) was studied exclusively.

The VLS growth mechanism could be defined as a process whereby liquid metallic droplets on top of substrates absorb growth species supplied in the vapor phase, and grow solid crystals underneath the metallic droplets. Since the first introduction of the VLS growth mechanism by R. S. Wagner and W. C. Ellis in 1964 [12], it has been widely studied and developed for NW growth over the past five decades.

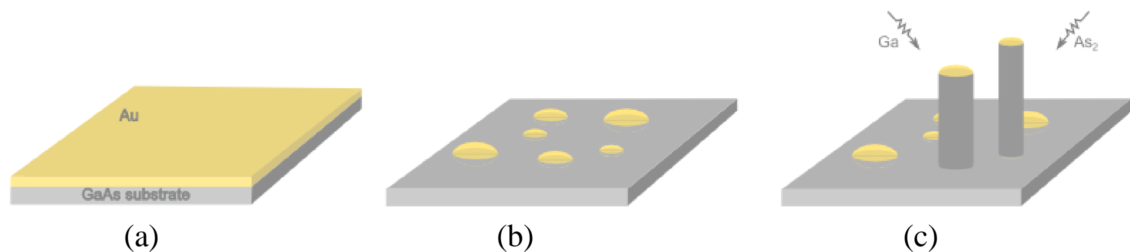

Figure 1.1. VLS mechanism for NW growth: a) a thin Au layer is firstly deposited on the GaAs substrate; b) the substrate is then transferred to an MBE system and heated to form Au droplets; c) Au droplets absorb growth species supplied in the vapor phase and grow GaAs crystals underneath.

At the beginning, a thin metallic impurity layer is deposited on a GaAs substrate (**Figure 1.1 (a)**). Both Ga [13] and Au [14] films have been reported being used as the seeding layer in NW growth by self-catalysing and foreign-catalysing methods, respectively. In this thesis, Au-catalysed NWs were studied exclusively. The substrate is then transferred into a molecular beam epitaxy (MBE) system and heated to a desired temperature. During the annealing process, the Au film alloys with group III atoms (Ga) from the substrate and form a eutectic alloy, which results in a lower melting point. Due to surface tension, the eutectic alloy nucleates into islands and form droplets (**Figure**

1.1(b)). For GaAs NW growth, the typical epitaxial growth temperature is around 600 ℃. At this temperature, Ga rich Au droplets are formed. Without pre-patterning of the substrate, Au droplets with different sizes are obtained, which eventually determine the diameter and height of grown NWs. Next, growth species (molecules or atoms of group III or group V elements) are supplied to the system in the vapor phase. Group V elements are supplied by hydride gas sources and pre-cracked into dimers before entering the chamber and then absorbed by Au droplets. AsH_3 is cracked into As_2 dimers for GaAs NW growth. Au droplets act as sinks that absorb atoms from direct impingement and surface diffusion on the substrate or NW sidewalls. The absorbed group III and group V atoms contribute to the Au droplets reaching a higher level of supersaturation, and incorporate to form crystals underneath the droplets (**Figure 1.1 (c)**). In this way, Au droplets stay on top of NWs and continuously grow GaAs crystals underneath with a constant supply of growth species.

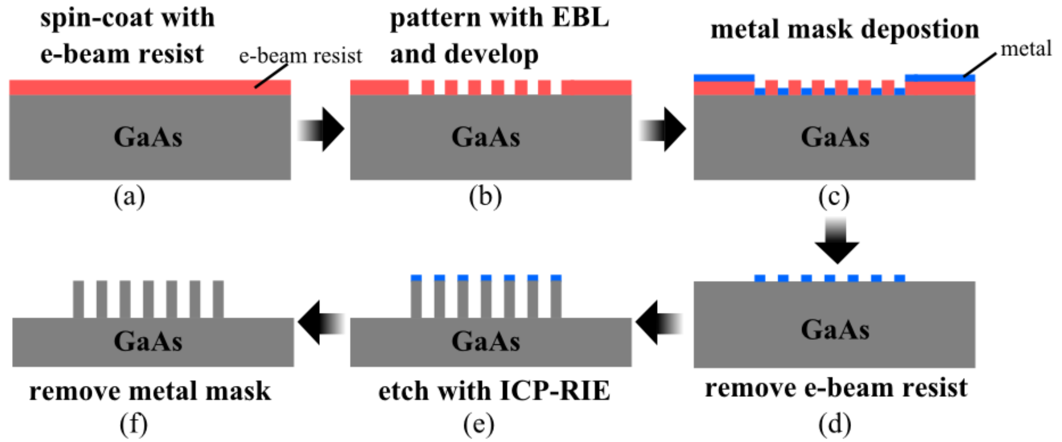

Figure 1.2. Top-down approach of obtaining NW arrays: a) a GaAs substrate is spin-coated with e-beam resist; b) the substrate is patterned with EBL and developed to remove resist exposed to the electron beam; c) a metal layer is deposited on the substrate; d) residual resist is removed; e) the substrate is etched with ICP-RIE to obtain NWs; f) the metal mask is removed with chemical etching.

Another technique used in NW fabrication is inductively coupled plasma reactive ion etching (ICP-RIE). In this technique, GaAs films or substrates are directly etched by high density plasma to obtain GaAs nanowires. As illustrated in **Figure 1.2,** an e-beam resist is firstly spin-coated on a GaAs substrate, followed by patterning with electron beam lithography (EBL). A metal layer is then deposited on top of the substrate, after which the residual resist is removed. Metals such as Al, Cr and Ni [15] have been reported being used as etching masks for GaAs nanowires in ICP-RIE. Besides, non-metal materials such as silica bead [16] have also been reported. After masking, the substrate is transferred into an ICP-RIE system and etched with high density plasma, such as Cl_2/N_2 [15], $Cl_2/SiCl_4/Ar$ [16], $Cl_2/N_2/BCl_3$ and CHF_3/Ar plasma [11]. Since the

plasma has a fast etching rate to GaAs and a very low etching rate to the mask, GaAs under the masks would not be etched. Depending on the size and spacing of the metal dots, NWs with different diameters and periods can be obtained. In Ref. [15], the top-down approach of GaAs nanowire array fabrication with ICP-RIE based on Cl_2/N_2 chemistry resulted in nanowires with 30 nm diameter and 1 μm length. In the work of Ke et al., nanowires with heights ranging from 540 nm to 2600 nm, and diameters from 200 nm to 400 nm were obtained [11]. The main advantage of this top-down approach is that the source material properties could be retained, and nanowires with different diameters and heights could also be easily controlled. It is a low-cost and robust sample preparation technique for achieving NW arrays.

1.2 Application of GaAs Nanowires

Due to excellent light absorption and high carrier mobility, GaAs nanowires are being widely studied for future optoelectronic applications. They have been reported in making laser diodes [17], photodetectors [18], and field effect transistors [19]. In Ref. [17], Hua et al. reported their GaAs/GaAsP core-shell NW laser diode grown by selective area metal organic vapor phase epitaxy (SA-MOVPE) has strong emission in the near-infrared range. Wang reported a GaAs nanowire-based photodetector that achieved a photoconductive gain of 20000 at low laser excitation [18]. More interestingly, GaAs nanowires are being widely studied in photovoltaic applications [20–28].

III-V multi-junction solar cells could achieve high efficiency under concentrated sunlight, but the high cost of III-V materials limit their applications in certain occasions. To reduce the cost by reducing the III-V material being used, III-V nanowire-based solar cells are being widely studied, especially in the last decade. Being one of the ideal materials, GaAs is promising in nanowire solar cells. In GaAs nanowire-based solar cells, p-n junctions can be created either within the nanowire [21, 22, 26] or between nanowires and the substrate [27]. By switching growth species and conditions during growth, nanowires can be controlled to grow axially or radially, and doped to n-type or p-type. In this way, heterostructures are created within nanowires to make p-n junctions. An alternative way is growing n-type nanowires on p-type substrate, or vice versa, to create p-n junctions between nanowires and the substrate. To increase solar cell efficiency, nanowires are usually passivated to reduce the density of states on the nanowire sidewalls. It can be achieved by chemical passivation with sulfur [23] or by encapsulating nanowires with a large band gap shell such as InGaP [21]. In literature, performances of both single nanowire solar cells and nanowire array solar cells have been reported. Han [28] and Colombo [24] reported their single GaAs nanowire solar cells with efficiencies of 2.8% and 4.5%, respectively. In Ref. [13], Krogstrup et al. reported an efficiency of 40% for their p-i-n GaAs nanowire solar cell, which is above the Shockley-Queisser limit. Further investigation indicated that the high efficiency is partly due to field concentration. The highest efficiency GaAs nanowire array solar cell was reported by Chao et al. in Ref. [25]. In their work, n-type GaAs nanowires were obtained by ICP-

RIE and embedded in P3HT to achieve 9.2% efficiency. GaAs nanowire array solar cells fabricated with MBE and selective area metalorganic chemical vapor deposition (SA-MOVPE) were also reported and their performances were summarized in **Table 1.1**.

Table 1.1. Summary of GaAs NW array solar cell performance.

Substrate	GaAs NW Structure	Fabrication method	η	FF	J_{sc} (mA/cm^2)	V_{oc} (V)	Illumin-ation	Ref.
n-GaAs (111)B	Core-shell	MBE	0.83%	27%	36.6	0.20	2.6 sun	[7]
p-GaAs (111B)	n-type	MBE	1.65%	25%	27.4	0.25	1 sun	[27]
n-GaAs (111B)	n-type; Embedded in P3HT	SA-MOVPE	1.44%	43%	18.6	0.18	1 sun	[20]
p-GaAs (111B)	Core-shell	SA-MOVPE	2.54%	37%	17.6	0.39	1 sun	[22]
n-GaAs (111B)	Core-shell; passivated with InGaP	SA-MOVPE	6.63%	62%	24.3	0.44	1 sun	[21]
n-GaAs (110)	n-type; embedded in P3HT	ICP-RIE	9.20%	70%	20.2	0.65	1 sun	[25]

1.3 Motivation of Present Work

For optoelectronic applications, the front contact should meet three requirements: high transmittance, low sheet resistance (high conductivity) and low contact resistance. Ni/Ge/Au contact is a traditional contact to n-type GaAs film and could achieve a specific contact resistivity as low as $\sim 10^{-6}\ \Omega\cdot cm^2$ [29]. However, its opaqueness prevents it from being used in optoelectronic devices. Transparent conducting oxides (TCOs), such as indium tin oxide (ITO) and aluminum zinc oxide (AZO) were then developed to contact

optoelectronic devices. Their applications have been found in both thin film devices [30] and nanowire devices [21, 22, 31–33]. Due to special properties of nanowires, existing TCO contacts have performed poorly on nanowire devices relative to thin film equivalents, and they could not achieve Ohmic contacts to GaAs nanowires. There are several criteria in contacting nanowires. Firstly, since nanowires have high aspect ratios, direct deposition of TCO materials onto the nanowire array would result in a high sheet resistance (large roughness) of ITO films. This issue has been reported in lowering conversion efficiency of InP nanowire solar cells in Ref. [31]. To lower the sheet resistance, gaps between nanowires should be filled with a material that is robust, transparent and insulating to support the contact layer. Secondly, the contact should have a low resistance to NWs with a small contact area. Mariani et al. reported their 630 nm thick ITO contact on GaAs nanowires supported by BCB polymer reached an excellent sheet resistance of 15 Ω/□ [22], but the high ITO/NW contact resistance resulted in a low fill factor of the solar cell. In order to improve the performance of optoelectronic devices, a contact with high optical transmittance and low contact resistance to nanowires should be developed. In this present work, an In/ITO contact with 13 Ω/□ sheet resistance, 0.13 $\Omega\cdot cm^2$ specific contact resistance and 89% transmittance has been developed to meet these requirements.

The second half of my work developed a technique to obtain substrate-free nanowire arrays and measure their absorption experimentally. Since light is coupled into nanowires at resonances [34], absorption of a nanowire array largely depends on the

diameter and length of nanowires, and the spacing between nanowires. Simulation work has shown the diameter and period dependence of the absorption of nanowire arrays [35]. To our knowledge, although the reflectance of nanowire arrays with different nanowire diameters and spacing has been determined experimentally [36], absorption of the nanowire arrays has not been determined directly yet due to inability in measuring transmittance. In this present work, a technique used to obtain substrate-free nanowire arrays with ICP-RIE and selective chemical etching is described. Absorption of nanowire arrays with different diameter-period combinations has been determined experimentally.

1.4 Introduction of Ohmic Contact

At the metal-semiconductor interface, charge carriers diffuse from one side to the other and create a depletion region. Based on Schottky's diffusion theory, a potential energy barrier, named as a Schottky barrier, would build up to block further diffusion of carriers. The barrier height ($q\varphi_b$) is approximately 2/3 of the band gap for n-type semiconductors and it is 1/3 of the band gap for p-type semiconductors [37]. In ref. [37], Rideout pointed out that there are three main mechanisms for carriers to transport from n-type semiconductor to the metal contact. They are: 1) thermionic emission (TE) of carriers that have sufficient energy to overcome the barrier height; 2) thermionic field emission (TFE) of hot carriers tunneling through the top of the barrier; and 3) field emission of carriers tunneling through the entire barrier (shown in **Figure 1.3**).

For thermionic emission, the current density (J) through the junction is determined by the barrier height $q\varphi_b$by Eq. 1.1:

$$J \propto exp\left(-\frac{q\varphi_b}{kT}\right) \exp\left(\frac{qV}{kT} - 1\right) \qquad \text{(Eq. 1.1)}$$

where k is Boltzmann's constant and T is the absolute temperature. In the case that the junction is forward biased, carriers gain energy to overcome the barrier and thermionic emission is enhanced.

The importance of thermionic field emission to thermionic emission is evaluated by the term kT/E_{00} , where E_{00} is proportional to the square root of doping density ($\sqrt{N}$). Increasing the doping density would reduce the barrier width (W_{dep}) and result in more carriers tunneling through the barrier. In this way, both thermionic field emission and field emission are enhanced.

The most common way to achieve an Ohmic contact is by placing a metal contact to a highly doped surface layer, in which quantum tunneling is enhanced. Ni/Ge/Au contacts have been studied for decades and proved to be one of the best contacts for n-type GaAs films by creating a highly Ge-doped GaAs region near the metal/GaAs interface [38]. When heating the as-deposited Ni/Ge/Au contact to 360 ℃, Ge and Au start to form a eutectic alloy [29], while Ni atoms diffuse into the GaAs film to create Ga vacancies. Then, Ge atoms fill the vacancies and create a highly doped surface layer at

the interface [38]. The Ni/Ge/Au contact has achieved a specific contact resistivity as low as ~10^{-6} $\Omega\cdot cm^2$ on GaAs films [29].

Another approach to form an Ohmic contact is reducing the barrier height to enhance the thermionic emission. This could be achieved by creating a graded band gap at the metal/semiconductor interface. Placing a graded InGaAs layer between the metal contact and GaAs film is a common way to achieve an Ohmic contact [39–42]. Lakhani has reported a specific contact resistance of 1.2×10^{-5} $\Omega\cdot cm^2$ that was achieved by heat treating a thick indium layer deposited on top of a GaAs film [40]. M. Murakami reported a technique that used In-based alloys, such as GeInW, NiInW [42] and MoGeInW [41], to achieve Ohmic contacts. The In-based alloys were deposited on GaAs films by evaporation and heat treated to form InGaAs layers. The reduced barrier height resulted in Ohmic contacts with specific contact resistances as low as 1×10^{-6} $\Omega\cdot cm^2$ [41]. A lower specific contact resistance of 5×10^{-9} $\Omega\cdot cm^2$ was reported by Nittono et al. In his work, the Ohmic contact was achieved by growing a graded InGaAs layer on a GaAs film with MBE [39]. However, the contacts introduced above are opaque and would not be suitable for GaAs NW devices that require transparent front contacts. Since it is also hard to grow highly doped GaAs NWs (>10^{19} cm^{-3}) in MBE, forming an Ohmic contact by enhancing thermionic field emission is difficult. In **Chapter 3,** a transparent In/ITO contact that achieved low resistance Ohmic contact to n-GaAs NWs by enhancing thermionic emission was introduced.

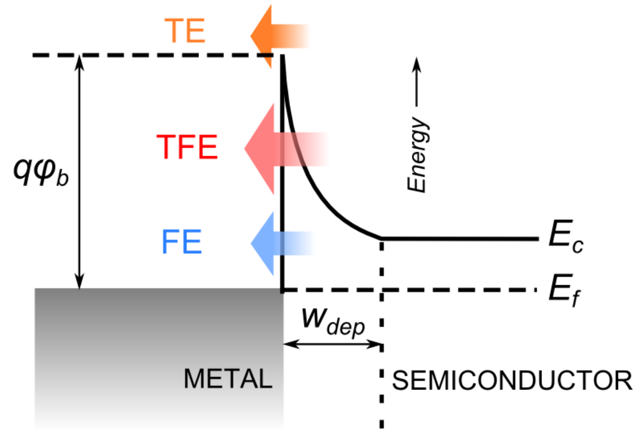

Figure 1.3. Schematic of band diagram at the metal/n-type semiconductor interface; and carrier transport mechanisms: thermionic emission (TE), thermionic field emission (TFE) and field emission (FE) from semiconductor side to metal side.

1.5 Introduction of Indium Tin Oxide (ITO)

Indium tin oxide (ITO), also named as tin doped indium oxide, is a solid solution that is typically composed of 90% indium oxide (In_2O_3) and 10% tin oxide (SnO_2) by weight. Bulk ITO materials can be formed by mixing In_2O_3 and SnO_2 powders [43] or doping In_2O_3 with Sn, in which process Sn atoms replace In atoms in the oxide compound [44].

Since ITO has a large band gap of ~4 eV [45], it was reported to have a transmittance as high as ~90% in the visible range [46], and very low transmittance in ultraviolet and infrared ranges in the light spectrum [47]. ITO was also reported to have an electrical resistivity as low as 10^{-4} Ω·cm [47]. Because of its high electrical

conductivity and optical transparency, ITO films are traditionally coated on aircraft windshields for defrosting purposes, and coated on display devices for antistatic purposes. More recently, ITO is widely used as transparent contacts for thin film devices and has found implementation in many NW devices. For example, ITO was used as a transparent contact on Si NWs to form metal-insulator-semiconductor (MIS) photodetectors [48], and formed transparent Ohmic contact to ZnO NWs in ultraviolet photodetectors [49]. ITO has also been widely used in contacting III-V semiconductor NWs such as InP NWs [32,50], and GaAs NWs [22,33] in NW solar cell applications.

ITO films could be deposited on samples through various techniques such as sputtering [51–54], screen printing [55], thermal evaporation [56] and spray pyrolysis [57]. Since the quality of ITO depends on many factors such as ITO grain sizes, density of impurities and surface roughness, ITO films obtained by different techniques have different characteristics. Sputtering is the most commonly used technique in ITO deposition for achieving high transmittance and low resistivity ITO films. In the sputtering process, atoms or molecules are knocked out from an ITO target by accelerated ions from excited plasma and reconstructed on the sample surface. Different sputtering techniques such as RF sputtering [51,52]; magnetron sputtering [53] and ion beam sputtering [54] have been reported in ITO deposition. A resistivity of $<10^{-3}$ Ω·cm was commonly achieved by sputter-deposited ITO films with thicknesses between 100 and 500 nm [51–54]. Compared to sputtering, spray pyrolysis has a faster deposition rate of >100 nm/s and could achieve a similar transmittance and conductivity. It is reported in

ref. [57] that a 550 nm think ITO film obtained by spray pyrolysis had achieved a resistivity of 3×10^{-4} Ω·cm and a transmittance of 85%. In screen printing, ITO films are usually a few tens of microns thick, which resulted in their relatively low transmittances. However, its ability in large scale deposition, as well as its fast processing rate, makes it suitable for applications in production lines.

In our work, ITO was sputtered from an ITO target that was composed of > 99.99% purity In_2O_3/SnO_2 (90/10 wt%) by argon plasma in a RF sputtering system. Since oxygen ions could be pumped out of the system before reaching the substrate, an oxygen gas flow was inlet into the chamber to compensate the loss of oxygen and maintain the transparency of deposited ITO films. Increasing in oxygen flow rate would result in an increase in transmittance and a decrease in conductivity, so an optimization of oxygen flow rate should be done to balance the transmittance and conductivity of the ITO film. As deposited ITO films usually have low conductivity because of large stacking faults, so they are usually heat treated to increase conductivity after deposition. In modern systems, substrates are heated during ITO sputtering so that stacking faults are reduced and low sheet resistances can be achieved.

2 Experiment

2.1 Electron Microscopy

The diameters of nanowires and the spacing between nanowires are on the order of tens or hundreds of nanometers. Since these values are so close to the wavelength of light in the visible range, nanowires cannot be resolved optically. However, electrons have a relativistic wavelength in the sub-Å range, which makes it possible to image nanowires with electron microscopy. In this work, two types of electron microscopes: scanning electron microscopy (SEM) and transmission electron microscopy (TEM) were used. SEM was mainly used in determining surface morphology of nanowires, such as nanowire sizes and densities, while TEM was incorporated with energy dispersive x-ray spectroscopy (EDS) to determine contact diffusion.

2.1.1 Scanning Electron Microscopy (SEM)

The JEOL JSM-7000F field emission scanning electron microscope (SEM) was used to determine the characteristics of samples, such as NW densities, cyclotene height and roughness of sample surfaces. The SEM is equipped with a tungsten filament cathode, which emits primary electrons by field emission. Primary electrons are accelerated in an

electric field and focused to a spot by condenser lenses. The objective lens, which determines the resolution of the instrument, then forms the focused electron beam into a small electron probe with a diameter of several nanometers. Scan coils deflect the electron beam in the x and y axes, so the electron probe could scan the specimen in two perpendicular directions to generate 2D images. At the probing spot, primary electrons interact with the sample and are scattered both elastically and inelastically within the interaction volume. The interaction volume depends on a few factors such as electron acceleration voltage and sample density. In inelastic scattering, part of the energy is lost in the energy exchange process and left with low energy secondary electrons. Those secondary electrons originated near the sample surface are able to escape from the sample and collected by an Evenhart-Thornley detector. In this detector, secondary electrons are converted into photons by a scintillator and the signal is amplified by a photomultiplier. In this way, by rastering the electron probe across the sample and detecting secondary electrons at each spot, a 2D image of the specimen can be generated.

Specimens can be mounted on either a 0 °(planar) stub or a 45 °stub depending on the morphological features to observe. To study the height of NWs or cyclotene, the specimen was usually mounted on a 45 ° stub with carbon tape, which allowed the specimen to be studied from 90 °to the NW axes. To study the density of NWs or surface roughness, it was preferred to mount the specimen on a 0 °stub and observe from 0 °, 30 ° and 45 °from the NW axis. For insulating samples, a 5 nm thick carbon layer was usually coated on sample surfaces to create a charge path to ground.

2.1.2 Transmission electron microscopy (TEM)

In order to determine the significance of indium diffusion into GaAs NWs or cyclotene, a high resolution JEOL 2010F transmission electron microscope (TEM) was used to analyze the sample prepared by focused ion beam (FIB) as described in section 4.2. In this TEM, electrons are emitted through field emission by applying a high electrostatic field at the tip of the cathode. The system was operated in scanning transmission electron microscopy (STEM) mode for imaging the sample. Similar to SEM, electrons are accelerated in an electric field parallel to the optic axis and focused to a spot by a condenser lens system. Since the sample is very thin, high energy incident electrons could either pass through the sample or scatter in the sample before getting collected by detectors. A high angle annular dark field (HAADF) detector was used to collect inelastically scattered electrons to image the sample. It is a large ring shaped detector placed under the specimen, and it also has a large collection angle to avoid collecting coherently diffracted electrons. The system is also equipped with an energy dispersive x-ray spectroscopy (EDS) detector, so chemical compositions at different locations on the sample could be determined. In EDS, an incident electron ejects a core shell electron and leaves a vacancy in the inner shell. An outer shell electron then fills the inner shell vacancy and emits an x-ray photon. The x-ray photon energy is characteristic of elements and it is determined by the energy levels of the inner and outer shells. Thus, by measuring the x-ray photon energy that has been detected, chemical compositions of the sample could be determined.

All the TEM images shown in this thesis were taken in the STEM mode with a 200 kV primary electron accelerating voltage. The position of the electron probe could be controlled by INCA software, and both EDS point-scan and line-scan measurements were taken by fixing the probe at a spot or scanning across the sample, respectively.

2.2 Secondary Ion Mass Spectrometry (SIMS)

In SIMS, primary ions generated by electron ionization, such as O_2^+ and Cs^+ ions, are accelerated in an electric field and focused to a spot by several condenser lenses. The primary ion beam size can be as low as ~1 μm in diameter [58]. The outermost layer of the sample surface is sputtered by the primary ion beam and ionized secondary particles are generated in this process. The ionized secondary particles pass through an energy filter to screen out particles in a narrow energy range and separated by a mass spectrometer according to their mass/charge ratios. The separated secondary ions are then detected by the detector to determine the element and chemical composition of the sample. Only a fraction of 10^{-6}-10^{-1} of the secondary particles is positively or negatively charged, so most of the particles are neutral atoms that are filtered out through the mass spectrometer and cannot be analyzed [59,60]. Since the sputtering rate of a certain material is constant, the secondary ion signal is recorded as a function of time throughout sputtering, and a depth profile could be generated at the end by simply measuring the crater depth. This fact makes in-depth analysis possible. SIMS can detect different

elements simultaneously and has a depth resolution of 1 to 5 nm [59]. Depending on the target sample parameters, type and size of primary ions beams, lateral resolution varies from less than 100 nm to a few microns [60].

2.3 Inductively Coupled Plasma Reactive Ion Etching (ICP-RIE)

An inductively coupled plasma reactive ion etching (ICP-RIE) system is equipped with two radio frequency (RF) sources: one creates high density plasma, the other accelerates the reactive species to etch the sample. Initially, reactive gases are inlet into a vacuum chamber and maintained at a desired chamber pressure. High density plasma is then initiated by applying a strong RF electromagnetic field to the gas cloud. Since the substrate is biased by the other RF source, reactive ions are extracted from the plasma and accelerated to etch the sample. By controlling the composition of gas mixture, chamber pressure and RF power, the etching rate could be altered.

To form nanowires, a substrate is firstly lithographically patterned and then etched with ICP-RIE. In our work, an Oxford PlasmaTherm ICP-RIE system was used to etch Al/Cr masked GaAs substrates. Firstly, an electron-beam (e-beam) resist (PMMA950-A3) was coated on the GaAs substrate and an array of dots was patterned by electron beam lithography (EBL) on the polymer. After that, the substrate was developed in methyl-

isobutyl-ketone to remove the resist that was exposed to the electron beam. After developing, the substrate was deposited with a thin layer of Al and Cr, followed by immersionin acetone to remove the residual resist. Since the metal layer deposited on top of the resist would also be lifted off, an array of metal dots was eventually left on the substrate. With this patterning technique, metal dots with different sizes and spacing could be achieved and NWs with various diameter and periods can be obtained. After patterning, the sample was transferred to the ICP-RIE system and etched by N_2/Cl_2 plasma. Since the plasma has a high etching rate to GaAs and a very slow etching rate to the Al/Cr mask, GaAs crystal underneath the metal mask would not be etched. In this way, GaAs NW arrays could be achieved. At last, the metal mask was removed by chemical etching.

2.4 Electrical characterization

Glass microscope slides were used as witness samples during In and ITO depositions to be used for sheet resistance and optical transmittance characterization. A standard four-point probe technique, shown in **Figure 2.1**, was used to measure the sheet resistance of the ITO and In/ITO films on the glass slides both before and after annealing.

A two-point probe configuration and a Keithley 2400 sourcemeter were used to obtain I–V characteristics between front and back contacts of the NW samples as

indicated in **Figure 2.1**. Specific contact resistances were then estimated from the I–V characteristics as described in Chapter 3.

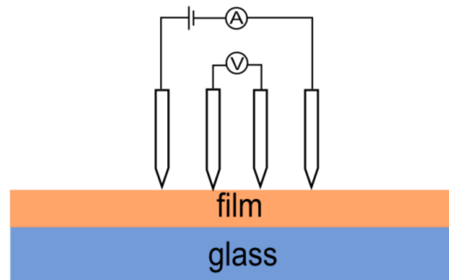

Figure 2.1. Schematic of sheet resistance measurement by four-point probe technique.

2.5 Optical characterization

Optical transmittance of the ITO and In/ITO films after annealing were measured by variable angle spectroscopic ellipsometry operated in transmission mode and normalized to the transmission through an uncoated microslide.

An optical system was setup for transmittance and reflectance measurements of nanowire arrays. An Ocean Optics LS-1 light source with tungsten halogen lamp was used as the light source in this setup. Source light was split by several beam splitters and focused onto the sample by a few lenses. Light reflected from the sample or transmitted through the sample was coupled into an optical fiber and analyzed by an Ocean Optics Jaz spectrometer. Before the reflectance measurement, the sample was replaced by a

mirror in the setup to calibrate the light source. Reflectance of nanowire arrays were normalized to the calibrated light and transmittance was normalized to the transmission through air. More details about the setup will be described in **Section 5.1.**

A Zeiss Axioplan2 light microscope (LM) that was equipped with a digital camera was used in checking sample status, such as determining sample size and etching-hole depth. Images with the LM working in both reflection mode and transmission mode were taken using Clemex Vision Lite software.

3 Low Resistance Indium Tin Oxide (ITO) Contact to n-GaAs Nanowires

3.1 Introduction

Due to their unique properties, GaAs nanowires (NWs) are being widely studied for future optoelectronic applications such as laser diodes [17], photodetectors [18] and solar cells [7,9] . As with thin film devices, these applications require electrical contacts which possess both low contact resistance and good transparency, thus precluding the use of established opaque contacts such as Ni-Ge-Au and Ti-Pt-Au to achieve low resistance, ohmic front contacts [61,62]. Transparent conducting oxides (TCOs), such as indium tin oxide (ITO) or aluminum zinc oxide (AZO), are typically used as transparent contacts for thin film devices and have found implementation in several NW devices. For example, ITO was used as a transparent contact on Si NWs to form metal-insulator-semiconductor (MIS) photodetectors [48], and formed transparent Ohmic contact to ZnO NWs in ultraviolet photodetectors [49]. ITO has also been widely used in contacting III-V semiconductor NWs such as InP NWs [32,63] and GaAs NWs [21,22] in NW solar cell applications.

Despite its popularity for both thin films and NWs, TCO contacts to NW devices have performed poorly relative to thin film equivalents, thus leading to performance degradation in NW devices. Among NW solar cells, a high sheet resistance [63] of the ITO top contact and high contact resistances between ITO and NWs [33] are believed to play a primary role in limiting conversion efficiency. Ref. [33], for example, reported a poor ITO/InGaAs NW contact resulting in a high parasitic resistance, which degraded the performance of photovoltaic devices. A 630 nm thick ITO contact possessed an excellent 15 Ω/□ sheet resistance but was reported to suffer from high ITO/NW contact resistance, which resulted in a low fill factor of the solar cell in Ref. [22]. AZO contacts also had a poor performance on the same NWs because of its higher sheet resistance (627 Ω/□). In comparison, a modified Ti/ITO contact applied to p-GaAs substrates reported a ~12.5 Ω/□ sheet resistance while achieving Ohmic contact on thin film calibration samples with doping densities as low as 1×10^{18} cm^{-3} in Ref. [21]. However, the performance of Ti/ITO contacts on NWs has not been specified. To our knowledge, the contact between ITO and NWs has not been thoroughly characterized nor optimized largely due to the infeasibility of extending established thin film characterization techniques to NWs. This present work describes the formation of ITO contacts on n-GaAs NWs which achieves high optical transmittance while simultaneously achieving low sheet resistance and low specific contact resistance.

3.2 Experimental Details

n-GaAs NWs were grown by the Au-assisted vapor–liquid–solid (VLS) method in a gas source molecular beam epitaxy (MBE) system on a n-GaAs wafer. The wafer was cleaned by UV ozone oxidation, followed by buffered HF etching and rinsing in deionized water. Afterwards, a 1 nm thick Au layer was deposited onto the substrate in an e-beam evaporation system. Samples were grown at a nominal 2D growth rate of 0.5 μm h^{-1} with a V/III flux ratio of 2.3 and a substrate temperature of 600 ℃ [4]. Two samples of different NW doping were grown to determine the influence of doping on specific contact resistance. Sample A NWs were grown for a duration of 30 min, and were n-doped by Te with a nominal carrier concentration of 5×10^{18} cm^{-3} as determined from previous Hall effect calibrations on (100) GaAs films. Sample B NWs were grown under the same conditions as sample A but with a nominal carrier concentration of 5×10^{18} cm^{-3} for 15 min followed by Te doping with a carrier concentration of 8×10^{18} cm^{-3} for 25 min. Hence, sample B was similar to sample A but with higher doping at the top of the NWs. The nominal doping was identical at the beginning of growth in sample A and B to avoid any doping dependent changes in growth mechanism that may influence NW density [64]. The structure schematic and SEM images of Sample A and B are shown in **Figure 3.1**.

Both sample A and sample B were spin-coated with cyclotene and baked for 30 min at 250 ℃ on a hot plate in N_2 ambient, so that the gap between NWs was filled by cyclotene to support the contact layer at the top of NWs. A controlled length of NWs was

exposed by back etching the cyclotene with CF_4 and O_2 plasma in a reactive ion etching (RIE) system. Samples were subsequently sonicated in DI water for 10 min using a Branson 1510 ultrasonic cleaner to remove the top of NWs exposed above the cyclotene layer. Hence, the Au seed at the top of NWs was removed. Finally, in preparation for top contact deposition, samples were cleaned by immersion in acetone for 9 min and methanol for 4 min, followed by rinsing with DI water for 6 min. This planarization process has been described in detail in [65]. A JEOL JSM-7000F scanning electron microscope (SEM) was used to determine the final height of NWs embedded in the cyclotene and the area coverage of NWs.

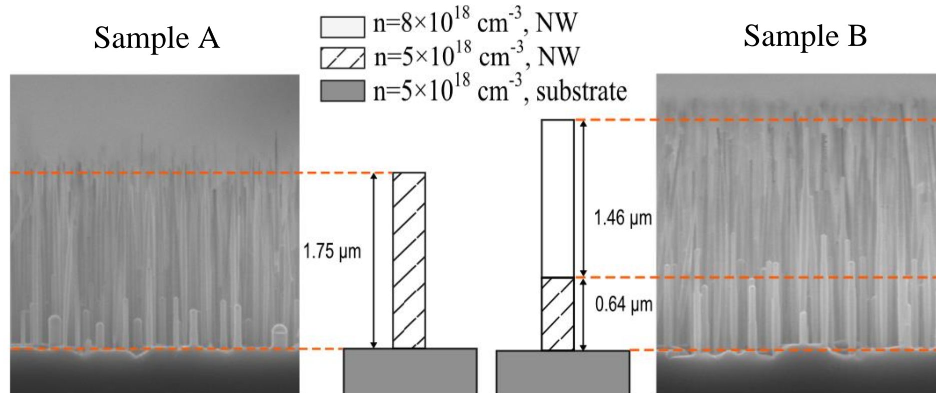

Figure 3.1. SEM images and structure schematics of NWs in Sample A and Sample B.

Four different contact pads were deposited on each NW sample as depicted in **Figure 3.2(a)**. Deposition through a shadow mask consisting of 2 mm diameter apertures was used to provide multiple TCO contact pads on the NWs and prevent short circuits at the sample edges. First, 25 nm thick indium (In) contact pads were deposited by RF

sputtering with 25 sccm argon (Ar) flow rate, 25 W RF power, and 7.2 mTorr chamber pressure. Vacuum tape was used to cover a fraction of the apertures in the shadow mask, such that only a portion of the sample received the In contact pads. Next, the vacuum tape was removed without disturbing the mask, and 500 nm thick ITO was deposited by RF sputtering with flow rates of 36 sccm Ar and 0.2 sccm O_2, power of 125 W, chamber pressure of 5 mTorr, and deposition rate of ~2 Å/s. In this manner, half of the contact pads consisted of ITO only (indicated as contacts C in **Figure 3.2(a)**), while the remaining half contained the In/ITO layer (indicated as contacts D in **Figure 3.2(a)**). To provide low probing resistance, Ni/Ge/Au (50/100/250 nm) was finally deposited by electron beam evaporation onto all of the In/ITO and ITO contact pads through a shadow mask with 1 mm diameter circular apertures. The resulting contact pads are indicated by configuration C and D in *Figure 3.2*(**a).** Ni/Ge/Au contact pads were also deposited directly on top of the NWs and the bare substrate (without NWs) for comparison with the In/ITO and ITO contact pads. The latter are indicated as configurations A and B in **Figure 3.2(a)**. Ni/Ge/Au (25/50/120 nm) was then deposited over the bottom of the samples by electron beam evaporation. The samples were then annealed for 30 s at 400 ℃ in N_2 ambient in a rapid thermal annealing (RTA) system to alloy the contacts to GaAs.

3.3 Results and Discussion

3.3.1 Contact Resistance

Two-point probe I-V measurements across the NWs were made to determine the specific contact resistances. First, the parasitic resistance of the two-point I-V measurement apparatus was determined by short circuiting the two-point probes. The I-V characteristic (not shown), measured with the two probes shorted, indicated a parasitic system resistance of $R_{sys} = 2\ \Omega$. Additionally, I-V characteristics of probe configuration A in **Figure 3.2(a)** exhibited the same resistance of 2 Ω, indicating a negligible probe-contact, substrate and rear contact resistance relative to R_{sys}. As such, the I-V curves measured for probe configurations B, C and D in **Figure 3.2(a)** were converted into J-V' curves shown in **Figure 3.2(b)** and **(c)** where $V'=V-IR_{sys}$ gives the voltage drop across the NWs and the top contact. The current density is given by $J = I / A$ where A is the interfacial contact area between the NWs and the TCO given by the product of the contact pad size and the percentage of the contact area in contact with the NWs. This percentage was determined for each sample by SEM measurements prior to contact deposition and typically ranged between 1.5 to 4.5%. The error bars in **Figure 3.2(b)** and **(c)** are standard deviations obtained from measurements on four contact pads across each sample.

With **Figure 3.2(b)** and **(c)**, the slopes of J-V' curves can be related to the specific contact resistance:

$$\left(\frac{dJ}{dV'}\right)^{-1} = A \cdot R_{NW} + r_c \qquad \text{(Eq. 3.1)}$$

where r_c is the specific contact resistance and R_{NW} is the effective resistance of the NW. Since it is difficult to determine R_{NW} due to surface depletion effects [66], it is assumed that $AR_{NW} << r_c$ such that r_c can be directly determined from the slope of curves in **Figure 3.2(b)** and **(c)**. This assumption serves to overestimate r_c since any contribution from the AR_{NW} term in **Eq. 3.1** would serve to lower the calculated r_c. Additionally, when comparing different contacts on the same sample, differences in J-V' curves can be attributed to differences in the top contact resistances (and not differences in R_{NW}). As discussed below, even with the overestimation of r_c, the In/ITO contacts give excellent performance.

From **Figure 3.2(b)** and **(c)**, the specific contact resistances were obtained and summarized in **Table 3.1**. For sample A, Ni/Ge/Au contacts gave the best contact resistance of 0.11 Ω·cm^2. It must be noted that identical Ni/Ge/Au contacts deposited on thin film calibrations yielded $r_c < 10^{-4}$ Ω·cm^2, further demonstrating the overestimation of r_c values in **Table 3.1** due to ignoring R_{NW}. In sample A, ITO contacts gave a high $r_c = 33$ Ω·cm^2, but insertion of an In layer between the GaAs and ITO improved r_c to 11

$\Omega \cdot cm^2$. We speculate that this improvement is due to In diffusing into n-GaAs forming a smaller bandgap InGaAs layer, which is also known to reduce the contact resistance in thin films [40]. The addition of In represents a 3x improvement in r_c over ITO, but r_c is still two orders of magnitude greater than Ni/Ge/Au contacts. This is likely due to the presence of a Schottky barrier (caused by insufficient doping) at the GaAs-TCO interface as evidenced by the assymetry and rectification in the J-V' curves of **Figure 3.2(b)**. This necessitates the implementation of high doping. This standard procedure of high doping for forming Ohmic contacts [37], is showcased by J-V' results of sample B.

Upon examination of highly doped sample B J-V' curves in **Figure 3.2(c)**, it is clear that the curves are less rectifying, indicating a reduced Schottky barrier width (due to the increased doping) allowing for field emission. Ni/Ge/Au contacts on sample B show only a small improvement since these contacts already gave ohmic contacts for the lower doped sample A. However, ITO and In/ITO contacts on sample B showed large r_c improvements, giving values of $r_c = 1.41$ $\Omega \cdot cm^2$ and $r_c = 0.13$ $\Omega \cdot cm^2$ respectively, rivalling the performance of the ohmic Ni/Ge/Au contacts. From these results, a nominal NW doping of 8×10^{18} cm^{-3} is needed to realize Ohmic contacts between In/ITO and n-GaAs NWs.

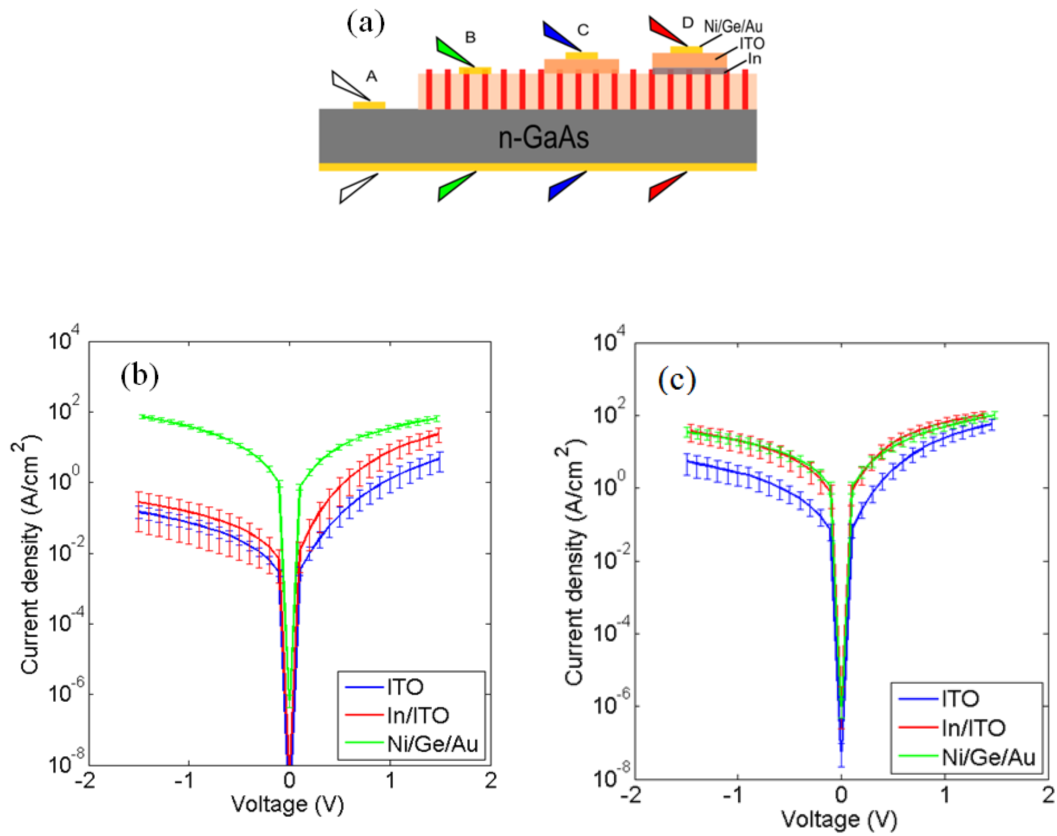

Figure 3.2. (a) Schematic of the different two-point probe configurations used for I-V measurements; (b) J-V' curves of different contacts on sample A; (c) J-V' curves of different contacts on sample B. The probe colors in (a) correspond to the curve colors in (b).

Table 3.1. Specific contact resistances for different contact materials on samples A and B.

	Specific contact resistance, r_c ($\Omega \cdot cm^2$)	
	Sample A (low doping)	Sample B (high doping)
Ni/Ge/Au	0.11	0.09
In/ITO	11	0.13
ITO	33	1.41

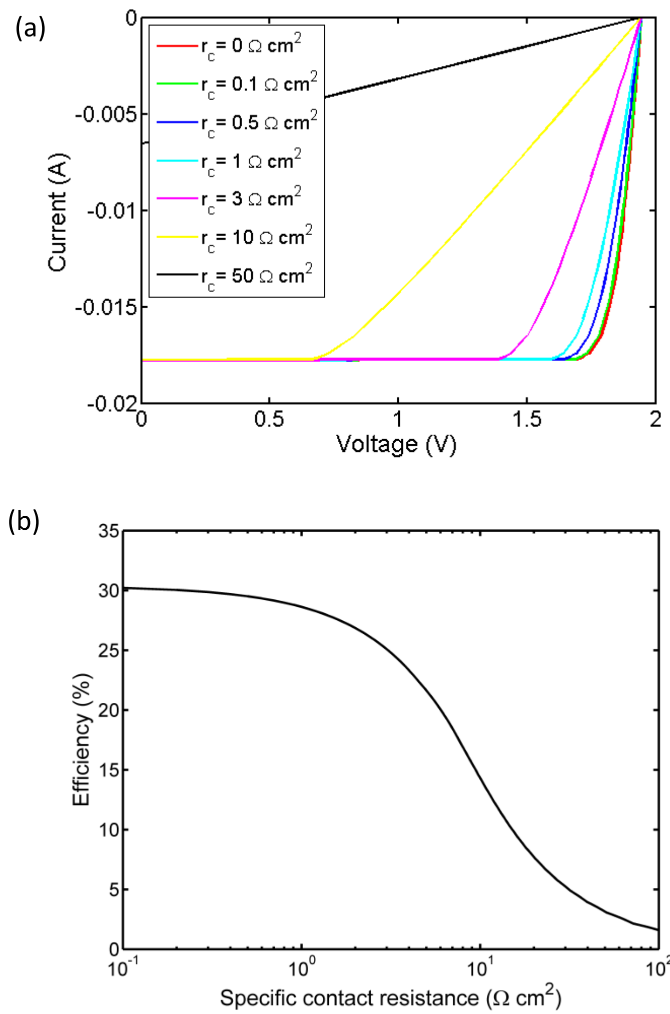

Figure 3.3. (a) Theoretical I-V curves for a photovoltaic device with various specific contact resistances, r_c. (b) Cell efficiency versus r_c extracted from the I-V curves in (a).

To assess the potential impact of this work, we estimated the effect of contact resistance on GaAs NW-based solar cells. The theoretical I-V characteristics under AM1.5G illumination for GaAs NW-based solar cells in Ref. [35] was modified to include a specific contact resistance (r_c) at the top of the NWs, and plotted in **Figure 3.3(a)**. From these I-V curves, the efficiency (η) of the cells can be extracted from η =

$I_{mp}V_{mp}/P_{inc}$ where I_{mp} and V_{mp} are the current and voltage at the maximum power point, and P_{inc}=100 mw/cm^2 for the AM1.5G spectrum. **Figure 3.3(b)** shows that significant efficiency degradation only occurs for $r_c > 1$ Ω·cm^2. Comparing this with **Table 3.1** shows that a high doping of 8x10^{18} cm^{-3} (sample B) is imperative to avoid severe efficiency degradation. Additionally, a supplemental In layer gives $r_c < 0.13$ Ω·cm^2 which is seen to yield a negligible impact on the photovoltaic device performance. Even without the In layer, the ITO contact is good enough provided the NW is doped higher than 8×10^{18} cm^{-3}.

3.3.2 Transmittance

According to the transmission results shown in **Figure 3.4**, the unannealed ITO and In/ITO film exhibited a low average optical transmittance of 81% and 63%, respectively, over a wavelength range of 400 to 900 nm. The post-annealing average transmittance of the In/ITO film increased to 89%, which is comparable with 91% for the ITO film (without In). The increase in transmittance after annealing of the In/ITO film results from diffusion of In into the ITO film. The annealing enhances the transmission in the ultraviolet range while drastically reducing the transmission in the infrared range.

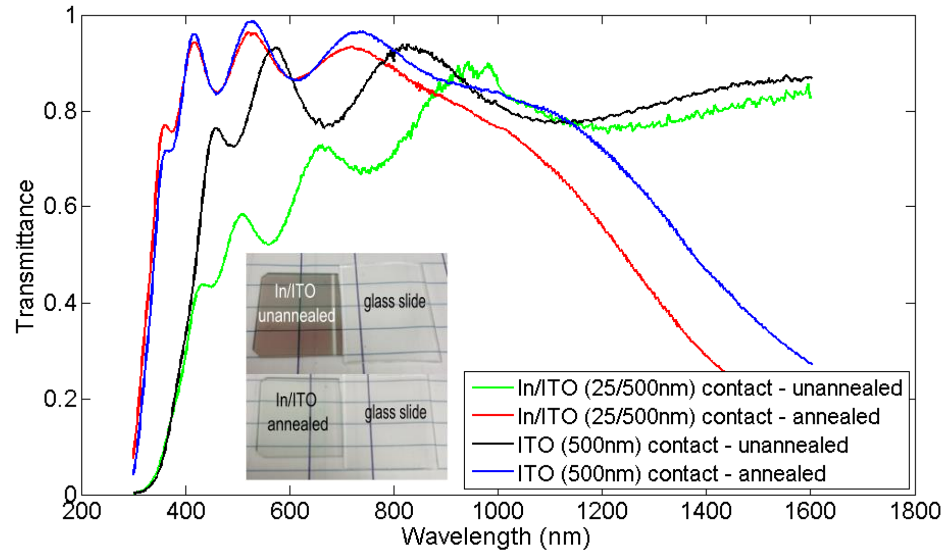

Figure 3.4. Optical transmittance spectrum of ITO and In/ITO films normalized to the glass slide transmission. The inset shows the unannealed (top) and annealed (bottom) In/ITO film on a glass slide, in comparison with a glass slide without deposition.

3.4 Sheet resistance

After optical characterization, sheet resistances of unannealed and annealed TCO films on glass slides, as measured by four-point probe, are tabulated in Table 3.2. As commonly reported for ITO [51], unannealed films had a very high sheet resistance while annealing reduced the sheet resistance to 21 Ω/□. The In/ITO film showed a lower sheet resistance before and after annealing compared to the ITO film. The annealed In/ITO film showed the lowest sheet resistance of 13 Ω/□.

Table 3.2. Sheet resistance of ITO film and In/ITO film on glass slide.

	ITO (500 nm)		In/ITO (25/500 nm)	
	Unannealed	Annealed	Unannealed	Annealed
Sheet resistance (Ω/□)	3.7×10^4	21	122	13

3.5 Contact pad crack test

As shown in **Table 3.3**, the difference in coefficient of thermal expansion (CTE) between ITO and cyclotene is large, which would cause the contact pads to crack after annealing. An example of an SEM image of cracks on an ITO contact pad after annealing is shown in **Figure 3.5.** In order to determine the largest size of a crack-free contact pad, contact pads with various sizes were deposited onto cyclotene-buried NW samples. The contact pads achieved by photolithography (PL) were square shaped with length of side varying from 150 µm to 600 µm. The technique used in In and ITO deposition was the same as described in **Section 3.2.** Crack test results are shown in **Table 3.4**. 250 nm thick ITO pads started to crack when the pad length increased to 300 µm, while none of the In/ITO (25/250 nm) pads cracked in the test. Since indium has a relatively low melting point of 157 ℃, it would melt when the sample was heated to 400 ℃. It was suspected that the indium layer acted like a "lubricant" that prevented the expanding cyclotene from stretching the ITO and tearing it apart. It was also possible that indium diffused into the ITO film and changed the composition of ITO, which resulted in a higher CTE.

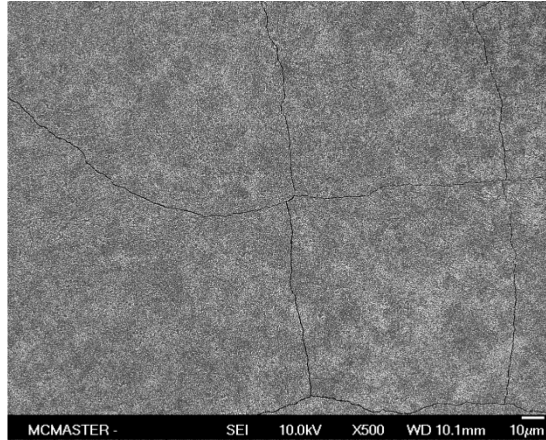

Figure 3.5. SEM image of cracks on ITO contact pad after annealing.

Table 3.3. Coefficient of thermal expansion (CTE) of several materials at room temperature.

	Cyclotene	ITO	In
CTE (ppm/ ℃)	42 [67]	8.5 [68]	~50 [69]

Table 3.4. Crack test results of various sizes of ITO (250nm) and In/ITO (25/250nm) square contact pads.

Length of side	150µm	200µm	250µm	300µm	350µm	400µm	500µm	600µm
ITO (250nm)	N	N	N	Y	Y	Y	Y	Y
In/ITO (25/250 nm)	N	N	N	N	N	N	N	N

*N – there are no cracks on the contact pad; Y – there are cracks on the contact pad.

3.6 Improved Contact Resistance on Etched NWs

Sample S4 (as described below) showed an improved contact resistance of In/ITO contact to GaAs NWs. Initially, a 500 nm thick GaAs epilayer with a carrier concentration of $8x10^{18}$ cm^{-3} was grown on a GaAs substrate. NWs in sample S4 were obtained by etching the GaAs epilayer with an inductively coupled plasma reactive ion etching (ICP-RIE) system with different diameters (D) and periods (P). Three different NW pads: 1) D=100 nm, P=350 nm; 2) D=180 nm, P=350 nm; and 3) D=300 nm, P=700nm, were all contacted with 25 nm thick In and 500 nm thick ITO. Details about sample processing methods will be introduced in **Section 4.2**.

Since NWs in sample S4 were shorter and thicker than those in sample A and B (**Section 3.2**), NW resistances (R_{NW}) would be even smaller. However, by assuming R_{NW} = 0, we would still overestimate r_c values calculated with **Eq. 3.1**. J-V' curves of In/ITO contacts on these three NW pads are shown in **Figure 3.6** and specific contact resistances (r_c) were obtained and summarized in **Table 3.5**. For the pad with D=100 nm and P=350 nm, the In/ITO contact had the highest r_c = 2.65 $\Omega\cdot cm^2$. However, when the diameter of NWs increased to 180 nm while the period remained the same, r_c was reduced to 0.70 $\Omega\cdot cm^2$. This fact indicated that the contact resistance is NW diameter dependent due to surface depletion effects [66]. The lowest r_c = 0.02 $\Omega\cdot cm^2$ was achieved when the NW diameter was increased to 300 nm and the period was doubled to 700 nm. This r_c value was even lower than we achieved on sample B (0.13 $\Omega\cdot cm^2$). However, NWs in sample B

had a typical diameter of ~50 nm, which is much smaller than 300 nm here. Again, the increase in NW diameter reduced the significance of the surface depletion effect on contact resistances. In the extreme case that NWs are thick enough to connect with each other, the pad would act like a thin film. In our measurement, the In/ITO contact had a negligible contact resistance on GaAs thin films that was beyond the resolution of our two-probe station. Another technique, such as transmission line method (TLM), has higher resolution that could be used to determine this very low specific contact resistance.

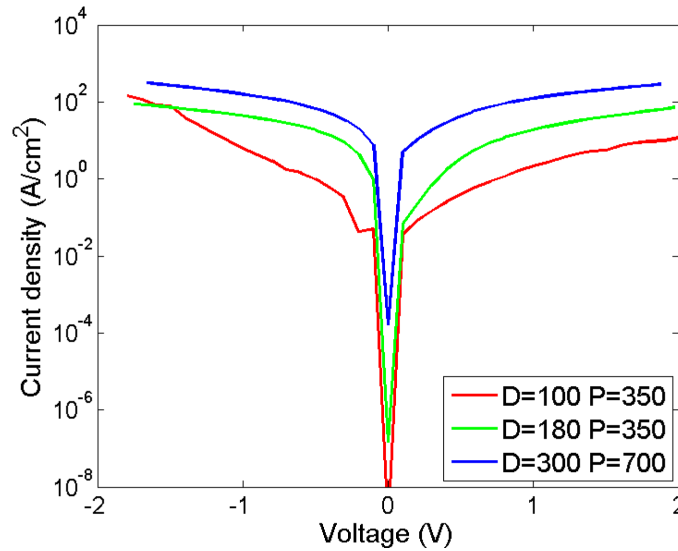

Figure 3.6. J-V' curves of In/ITO contacts on GaAs nanowires with D=100 nm, P=350 nm; D=180 nm, P=350 nm; and D=300 nm, P=700nm.

Table 3.5. Specific contact resistance of In/ITO contacts on GaAs nanowires with D=100 nm, P=350 nm; D=180 nm, P=350 nm; and D=300 nm, P=700nm.

	D=100 P=350	D=180 P=350	D=300 P=700
r_c ($\Omega\cdot cm^2$)	2.65	0.70	0.02

3.7 Contact Test on Planar GaAs Solar Cells

In order to assess the impact of low resistance contacts on solar cells, performance of both In/ITO and ITO contacts on planar GaAs solar cells were evaluated as shown in **Table 3.6.** *Thin film GaAs solar cell structure.* Five epilayers were grown on a p-type GaAs (100) substrate in a gas source molecular beam epitaxy (MBE) system. The GaAs substrate was Zn-doped and had a carrier concentration of $n>5\times10^{18}$ cm^{-3}. Firstly, a 50 nm thick Be-doped GaAs (p-type) buffer layer with a carrier concentration of 3×10^{18} cm^{-3} was grown on the substrate, followed by a 70 nm thick Be-doped InGaP back surface field (BSF) layer with $n=1\times10^{18}$ cm^{-3}. After that, a 1.5 µm thick p-type GaAs base film (Be-doped, $n=1\times10^{17}$) and a 100 nm thick n-type GaAs emitter film (Si-doped, $n=3\times10^{18}$) were grown to create a p-n junction. In order to achieve a good front contact, a 30 nm thick n-type GaAs film doped to $n=1\times10^{19}$ cm^{-3} with Si as dopants was grown on top of the sample.

Table 3.6. Thin film GaAs solar cell structure.

Layers	Doping	Thickness
n^+-GaAs (contact)	Si: 1x10^{19} cm^{-3}	30 nm
n-GaAs (emitter)	Si: 3x10^{18} cm^{-3}	100 nm
p-GaAs (base)	Be: 1x10^{17} cm^{-3}	1.5 µm
p-InGaP (BSF)	Be: 1x10^{18} cm^{-3}	70 nm
p-GaAs (buffer)	Be: 3x10^{18} cm^{-3}	50 nm
p-GaAs (100) substrate	Zn: >5x10^{18} cm^{-3}	350 µm

To evaluate the contacts, ITO (250 nm) and In/ITO (25/250 nm) contact pads were applied on two planar GaAs solar cells, respectively. Ni/Ge/Au (50/100/250 nm) bus bars were deposited on top of the contact pads by electron beam (e-beam) evaporation to reduce probing resistance. A control sample with Ni/Ge/Au bus bars directly deposited on top of the cell was processed at the same time. The back of the samples were contacted with Ti/Pt/Au (25/50/100 nm). Structure and appearance of the samples after contacting are shown in **Figure 3.7(a)** and **(b)**, respectively. Samples were annealed for 30 s at 400 ℃ in a rapid thermal annealing (RTA) system before I-V measurement. I-V characteristics were measured by two-point probe configurations with a Keithley 2400 sourcemeter under an AM1.5G spectrum. J-V' curves of the solar cells contacted with ITO, In/ITO and Ni/Ge/Au are shown in **Figure 3.8**.

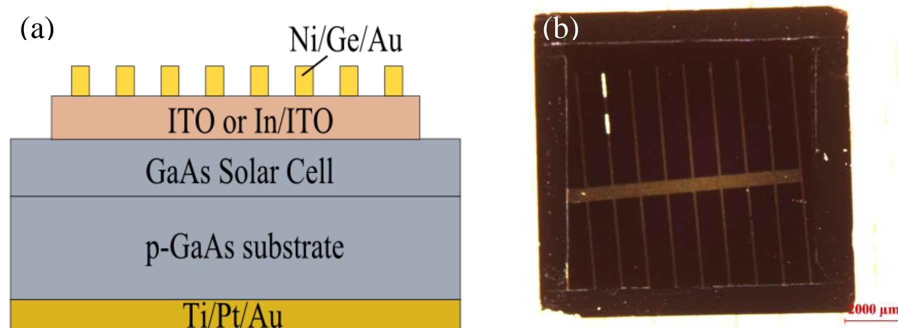

Figure 3.7. (a) Schematic and (b) light microscope image of planar GaAs solar cells contacted by ITO (or In/ITO) pad and Ni/Ge/Au fingers.

Among the three solar cells, the control sample (Ni/Ge/Au) had the lowest open circuit voltage (V_{oc}) of 0.40 V and the lowest short circuit current (J_{sc}) of 13.64 mA/cm^2. The low V_{oc} and J_{sc} resulted in its low efficiency of only 1.74%. Both In/ITO and ITO

contacted solar cells had similar V_{oc} *and* J_{sc}. The solar cell contacted by ITO had a J_{sc} of 20.47 mA/cm^2 and a V_{oc} of 0.73 V, while the cell contacted by In/ITO had a J_{sc} of 20.91 mA/cm^2 and a V_{oc} of 0.78 V. The fill factor (*FF*) for In/ITO contacted cell was 44.62%, which was much higher than 38.37% for the ITO contacted cell. Compared to the conversion efficiency (η) of 5.38% obtained by the ITO contacted solar cell, the cell contacted with In/ITO had a higher η of 6.83%. The fact that the solar cell efficiency improved by inserting a thin indium layer between ITO and GaAs NWs indicated that the In/ITO contact had a lower contact resistance to NWs than ITO. This fact was also predicted by the model shown in **Section 3.3.1**. In section 3.3.1, we predicted that indium diffused into GaAs NWs and created a graded InGaAs layer to reduce contact resistance, but we did not know how far indium diffused into GaAs NWs. However, the result achieved on planar solar cells was evidence that indium diffusion length is less than 130 nm, otherwise it would have shorted the p-n junction and resulted in a decrease in conversion efficiency. Although the indium diffusion in the In/ITO contact resulted in a better result than the ITO contact on planar solar cells, we could not conclude that indium diffusion would not be a problem for GaAs NW devices because it was still possible that indium could diffuse along the NW sidewalls and potentially short the p-n junctions in the NWs. Thus, a contact diffusion test was carried out to determine the significance of indium diffusion into NWs, as discussed in detail in **Chapter 4**.

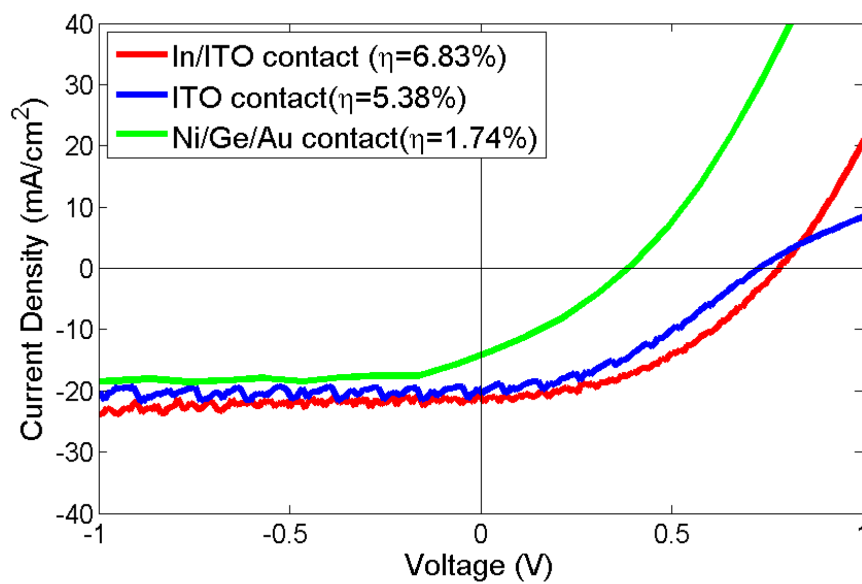

Figure 3.8. J-V' plots of planar GaAs solar cells contacted with Ni/Ge/Au, In/ITO, and ITO contacts under AM1.5G illumination.

4 Contact Diffusion Test

4.1 Introduction

Lakhani reported an indium-based Ohmic contact to GaAs films by creating a graded InGaAs layer [40]. In his work, a 600 nm thick indium layer was deposited on a GaAs substrate, followed by annealing for 60 s at 350 ℃. Graded InGaAs layers were found at several spots on the sample, but the indium diffusion length was not specified. Indium diffusion length is crucial in NW devices, such as NW solar cells, NW photodetectors and NW lasers, where p-n junctions or quantum dots are created within the NWs. There are two possible ways of indium diffusion in NWs: bulk diffusion in NWs and surface diffusion along NW sidewalls. If indium diffuses deep into NWs by bulk diffusion, it would potentially destroy the p-n junctions or quantum dots in the NWs. Long surface diffusion length would also possibly short axial p-n junctions and result in low NW solar cell efficiencies.

4.2 Experimental Details

Using the pre-growth preparation technique described in **Section 3.2**, an n-type GaAs (100) wafer was cleaned by UV ozone oxidation, followed by buffered HF etching

and rinsing in deionized water. A GaAs thin film was grown at a nominal 2D growth rate of 0.5 μm h^{-1} with a V/III flux ratio of 1.5 and a substrate temperature of 575 ℃. The 500 nm thick grown GaAs film was Te doped and had a carrier concentration of 8×10^{18} cm^{-3}. The grown GaAs film was then etched with inductively coupled plasma reactive ion etching (ICP-RIE) to obtain GaAs NWs.

For the NW etching process, a thin layer of e-beam resist (PMMA950-A3) was first spin-coated on the GaAs film. It was then baked at 180 ℃ for 20 min to cure the resist. After that, the resist was patterned by electron beam lithography (EBL) and developed in a methyl-isobutyl-ketone:isopropanol (1:3) solution [70]. Next, a 20 nm thick Al layer and a 45 nm thick Cr layer were deposited onto the sample by electron-beam evaporation. Finally, acetone was applied to the sample to lift-off the resist. The etching process was done in an Oxford PlasmaTherm ICP-RIE system with 10 mTorr chamber pressure, 20 sccm Cl_2 flow rate, 5 sccm N_2 flow rate, and a RF source power of 500 W. This sample was named as sample S4.

Sample S4 was processed to make a device and contacted by In/ITO (25/500 nm) and Ni/Ge/Au (50/100/250 nm) films with the methods described in **Section 3.6**. The sample was then annealed for 30 s at 400 ℃ in an RTA system to improve the contact. A Zeiss NVision 40 focused ion beam (FIB) was used to prepare samples for TEM analysis. The instrument was equipped with a gallium liquid-metal ion source (LIMS) and a Schottky field emission gun (FEG) filament scanning electron microscope (SEM).

Gallium atoms were ionized under a very high electric field. Ga^+ primary ions were then accelerated through an electric field and bombarded the sample to sputter an amount of material. The sputtering rate could be altered by changing the primary beam current, and precision milling to the nanoscale could be achieved at low primary ion beam currents. The entire milling process could be monitored by built-in SEM.

Initially, a 1.7 μm thick carbon layer was coated on 7 rows of NWs in the sample for protection and charge dissipation purposes. The surroundings of the carbon coated area were then milled by focused Ga ion beam to release the specimen from the bulk sample. The specimen was then transferred to a TEM grid and milled to only have one row of NWs left. The sidewalls of the last row of NWs were also partly milled so that the sample would be suitable for determining indium diffusion. The initial stage and final stage of the FIB process are shown in **Figure 4.1(a)** and **(b)**, respectively.

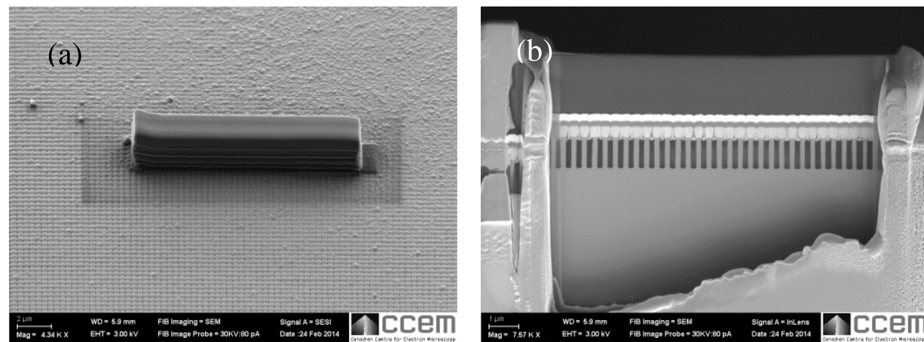

Figure 4.1. a) Initial stage and b) final stage of sample preparation for TEM with FIB.

4.3 Results and Discussion

To ascertain the indium bulk diffusion length in GaAs NWs and in cyclotene, EDS line-scans were taken across both the NW/contact interface and the cyclotene/contact interface (**Figure 4.2(a)**). At the NW/contact interface, Ga and As counts were low at the noise level in the contact region and they increased to a high level in the NW region, while In and Sn counts dropped tremendously, suggesting there is no significant bulk diffusion of either In or Sn. In and Sn counts also dropped rapidly to noise level at the cyclotene/contact interface, which means the diffusion into cyclotene was also not significant. In addition, since there was no abrupt In peak near the interfaces and Sn counts remained high across the contact region until the interfaces, it seemed that the deposited In film also diffused into ITO.

EDS line-scans were also taken at 50 nm and 100 nm below the NW/contact interface. In both cases, Ga and As counts peak in the middle of the NW region, while In counts stayed at noise level throughout the scans. Since not all cyclotene on the NW sidewalls got milled by FIB, residual cyclotene on either side of the sample contributed to oxygen and silicon counts in the EDS analysis. This reason explained the fact that silicon counts decreased at the cyclotene/NW interface but stayed at a level above the noise level.

In EDS point scans, 9 spots ranging from 36 nm above the NW/contact interface (in the contact region) and 141 nm below the interface were analyzed to find the change in chemical composition. **Figure 4.3** shows the atomic percentage of Ga, As and In in each

spot in the EDS point scan. Since ~150 nm tall NW tips were buried in the In/ITO contact, Ga and As at 36 nm above the interface had an atomic percentage of 26.78% and 25.92%, respectively. At this spot, In from the annealed In/ITO film contributed to the In counts, which resulted in 41.64%. Tin from ITO, oxygen from both ITO and cyclotene, and silicon from cyclotene contribute to the remaining 5.66%. At the interface, Ga and As percentages increased to 42.53% and 28.3%, respectively, while In dropped to 10.49% because of diffusion into both ITO and GaAs NWs. The slight increase in In percentage at a depth of 18 nm below the interface might have resulted from the rough cyclotene surface near the NW, where the original indium film was not uniform. From 36 nm below the interface, In percentage dropped gradually from 2.6% to 0% at a depth of 177 nm, while Ga and As percentages increased gradually to 48.16% and 47.98%, respectively. At the last spot, oxygen and silicon from cyclotene contribute to the other 3.86%. Hence, very little In could diffuse this far and In counts at this spot is below the detection limit of EDS. In other words, indium diffusion length is a maximum of 148 nm to 177 nm after heating for 30 s at 400 ℃.

However, EDS has a detection limit of 0.1~1% [71], corresponding to 10^{19} ~ 10^{20} atoms/cm^{-3}. Indium atoms below this density would still be able to short p-n junctions or destroy quantum dots in NWs, which means EDX is not sufficient to determine whether the indium diffusion is significant or not. An alternative technique, secondary ion mass spectrometry (SIMS), could be used to detect lower indium densities, as well as

generating a detailed depth profile. SIMS has a detection limit as low as 10^{14} cm^{-3} [59], which is sufficient for our purpose. This is recommended for future work.

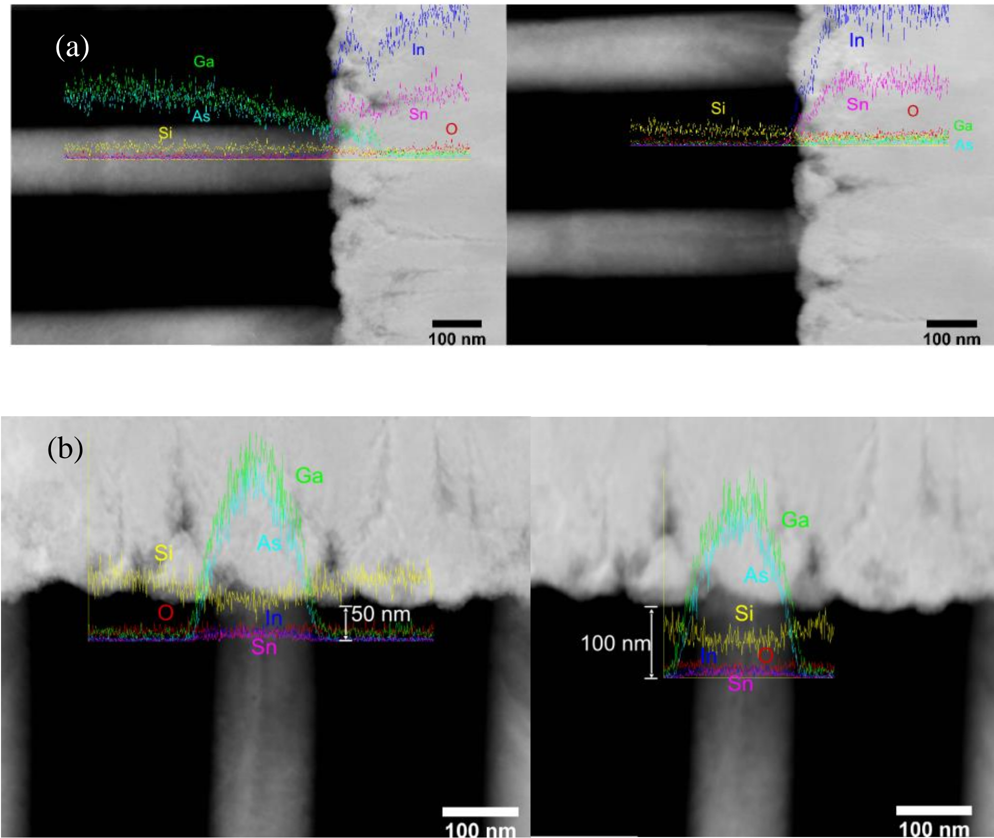

Figure 4.2. EDS line scan a) along NW; b) across the contact/cyclotene interface; c) across the NW at a depth of 50nm; and d) 100 nm under contact layer.

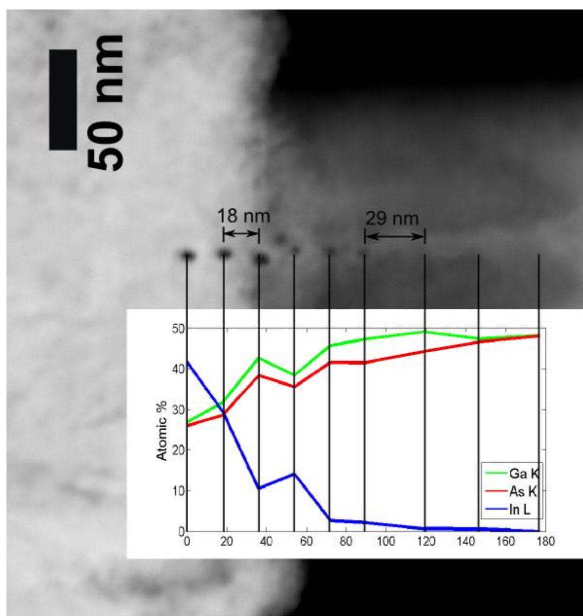

Figure 4.3. STEM image of NW/contact interface. Inserted 2D line plot shows the atomic percentage of Ga (green), As (red) and In (blue) at each scan spot in the EDS point-scan.

5 Transmittance and Reflectance of Nanowire Arrays and Thin Film

5.1 Introduction

As NW solar cells have excellent light trapping and use less materials compared to planar solar cells, optical properties of NW arrays are being widely studied for maximizing light absorption [34,35,72–74]. In NW arrays, light is coupled into NWs at resonances [34]. Hence, absorption of NW arrays could not be simply calculated with material properties. Other parameters, such as NW diameters (D) and space between NWs (P) should also be taken into consideration in determining absorptance of NW arrays. These parameters determine the resonance modes of light coupled into NW arrays. Finding out absorption of NW arrays would be crucial for NW based optoelectronic devices, such as solar cells and photodetectors. To maximize absorption, some simulation work has been done to optimize the diameter-period configurations for different material NW arrays [35,72]. In Ref. [72], Wen reported that the reflection and transmission should be traded off to maximize the absorption. More specifically, GaAs NW arrays tend to absorb more long wavelength photons (>700 nm), while having higher reflectance at short wavelength photons (<700 nm) with increasing fill factors (D/P). In addition, NWs with small diameters would have low reflectance, but absorptance would also be

low because fewer modes could be supported. In contrast, NWs with larger diameters could support more modes, but reflectance would also be increased [34,72]. In Hu's model, NWs with various diameters and periods were evaluated to maximize the absorption. An optimum D-P configuration for high efficiency two-junction GaAs nanowire-on-Si solar cells was obtained in his model [35]. Transmittance measurement of a NW array was firstly done by Sivakov on Si NW solar cells [74]. In his work, amorphous Si (a-Si) films were firstly deposited by electron beam evaporation (EBE) on a glass substrate. Then the Si layers were etched by electroless chemical etching with silver nitrate ($AgNO_3$) and hydrofluoric acid (HF) to obtained Si NWs. In this way, by measuring transmittance and absorptance of the NW array, absorptance of the NW array could be determined. However, absorptance or transmittance of GaAs NW arrays has not been determined experimentally yet because of difficulties in obtaining high quality substrate-free NW arrays. In this section, techniques that made these measurements possible are reported, as well as absorption results of GaAs NW arrays with various D-P configurations.

5.2 Experimental Details

To measure the transmittance of a NW array, the thick opaque substrate should be removed and the substrate-free NW array should be flat and well supported. One approach is covering the NW array with polymer (eg. PDMS), and then peeling the

polymer off [75]. This method could achieve high transfer yield, but NWs would break or be tilted during transfer. An alternative way is bonding the NW array to a glass microslide and etching the substrate off. However, both dry etching (by RIE) and wet etching (by chemical solutions) have relatively fast etching rate (~1μm/min), and caused difficulties in controlling etching depth. Since NWs and substrate are both made of GaAs, and the height of NWs (~2 μm) is quite small when compared to the substrate (>300 μm), slight over etch would destroy the NWs. The solution to this problem is inserting an etch stop layer between the GaAs substrate and GaAs NWs, and using selective chemical etching to remove the substrate without affecting NWs. In this section, techniques of forming NWs on an etch stop layer and methods of preparing samples for transmittance measurement are described.

5.2.1 GaAs Substrate Etching

One piece of the same planar solar cell that was described in **Section 3.7** was used in this absorption study. This sample was named as S5 and its structure is shown in **Figure 5.1(a).** S5 was coated with a metal mask and etched with ICP-RIE to obtain GaAs NW solar cells with methods discussed in **Section 4.2**. A schematic and SEM image of the GaAs NW solar cell after etching is shown in **Figure 5.1(b)** and **(c),** respectively. Sixteen NW pads were obtained with 100 μm × 100 μm size each and separated by a

spacing of 100 μm. Each pad had unique NW diameters and periods, and these parameters are listed in **Table 5.1**.

After etching, sample S5 was spin-coated with cyclotene for 60s at 5000 rpm to fill the gaps between NWs and to planarize the top surface. Cyclotene was then cured by baking in N_2 ambient for 30 min at 250 °C. To expose the top of NWs, cyclotene was etched back with CF_4 and O_2 plasma in a reactive ion etching (RIE) system. The Al/Cr top was removed by MF319 before contacting. Each NW pad was contacted by a 140 μm×140 μm In/ITO contact pad with 25 nm thick In and 500 nm thick ITO, followed by a Ni/Ge/Au (50/100/250 nm) ring (15 nm wide) deposited at the ITO pad edge. Details about contact depositions were discussed in **Section 3.2**. I-V characteristics of sample S5 were measured both before and after annealing as presented in Chapter 4 (S5 similar to sample S4 as described in Chapter 4).

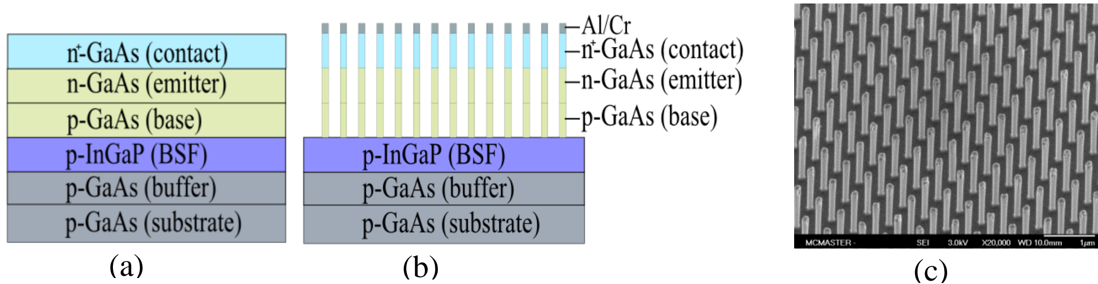

Figure 5.1. Schematic of a) a thin film GaAs solar cell structure grown by MBE; b) GaAs NW solar cell structure after etching with ICP-RIE; c) SEM image of an etched NW array (NW diameter =150nm, pitch = 350nm).

Table 5.1. Diameters and pitches of NWs in different pads in sample S5.

D1 D = 225 nm P = 270 nm	**C1** D = 225 nm P = 350 nm	**B1** D = 225 nm P = 460 nm	**A1** D = 225 nm P = 530 nm
D2 D = 180 nm P = 270 nm	**C2** D = 180 nm P = 350 nm	**B2** D = 180 nm P = 460 nm	**A2** D = 180 nm P = 530 nm
D3 D = 150 nm P = 270 nm	**C3** D = 150 nm P = 350 nm	**B3** D = 150 nm P = 460 nm	**A3** D = 150 nm P = 530 nm
D4 D = 110 nm P = 270 nm	**C4** D = 110 nm P = 350 nm	**B4** D = 110 nm P = 460 nm	**A4** D = 225 nm P = 570 nm

Sample S5 was bonded to a glass slide with EPO-TEK 301-2 epoxy, a transparent epoxy with a refractive index of 1.5 that has been reported being used in a wafer bonding process in multi-junction solar cells [76]. The epoxy was firstly applied to a glass microslide and spread uniformly, followed by pressing the sample against the glass microslide with sample front surface facing the glass. After that, the whole stack was baked in an oven at 80 ℃ for 3 hours to cure the epoxy. In this way, the epoxy could strongly hold the sample on the glass.

An etch window was opened on the back side of the substrate. The etch window was carefully aligned to the NWs on the other side of the substrate. In this process, the back contact in the middle of the substrate was firstly scratched off to expose the GaAs substrate. Then the sample was spin-coated with photoresist S1818 at 4000 rpm for 30s, followed by baking on a hotplate at 90 ℃ for 2 min to cure the photoresist. After that, sample S5 was transferred into a mask-aligner to expose the window area with 4.6 mJ/s

of UV light for 32.6 s. After exposure, the sample was immersed in toluene for 6 min, followed by baking at 90 ℃ for 45 s to make the surface of unexposed photoresist harder and resistant in developing. The sample was developed in MF 319 for 75 s to remove the photoresist for the etch window. The sample was then rinsed in running de-ionized (DI) water for 2 min and dried with a nitrogen gun before etching. **Figure 5.2** shows the schematic (**Figure 5.2(a)**) and images (**Figure 5.2(b) and (c)**) of sample S5 after bonding and photolithography (PL).

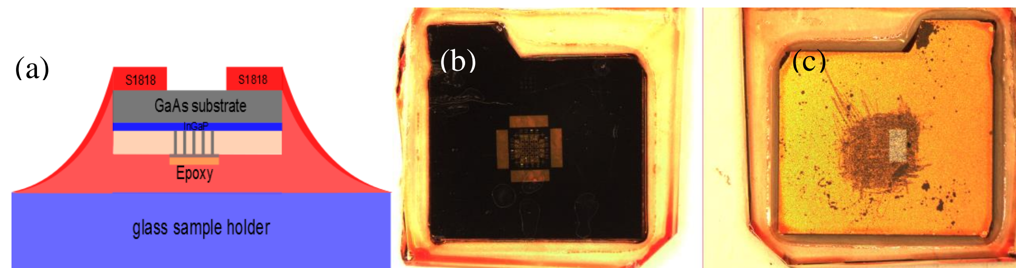

Figure 5.2. a) Schematic of sample structure; light microscope image of b) sample front surface; and c) sample back surface after bonding and PL.

The GaAs substrate in the etch window was etched by H_2SO_4:H_2O_2:H_2O (1:1:10) solution [77] at room temperature. This etchant was quite selective and it could etch GaAs at a fast rate, while etching InGaP at a very slow rate. The GaAs etching rate varied through the etching process as shown in **Figure 5.3**. The etching rate was ~4 μm/min at the beginning, and it decreased to ~1.5 μm/min after 130 min of etching. We suspect that as the etching hole got deeper, less chemical could reach the GaAs surface and less material could escape. The depth of the etching hole was measured by alpha-step when

etching time was less than 30 min, and it was measured by light microscope after 30 min of etching.

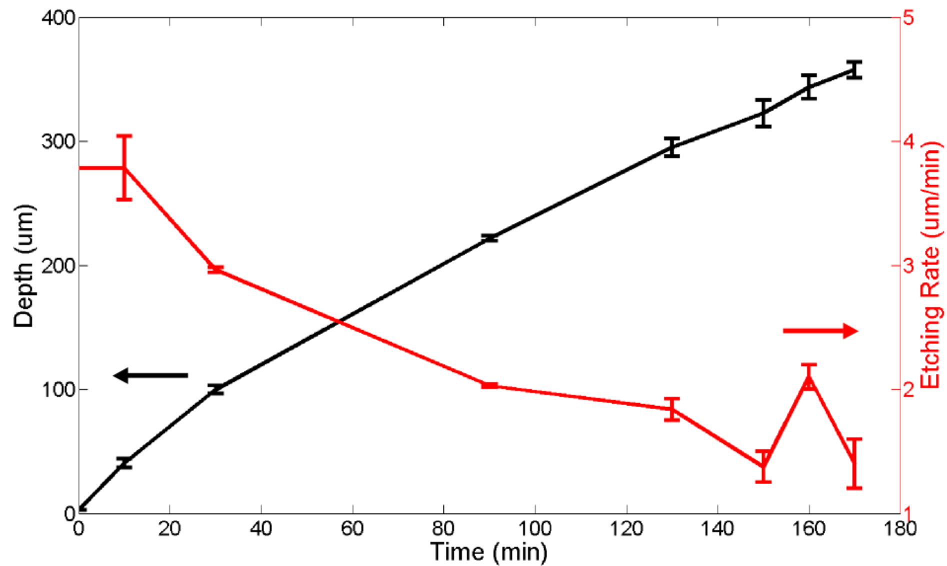

Figure 5.3. Etching rate and etching depth versus etching time.

As shown in **Figure 5.4**, light microscope images in both reflection and transmission modes showed that etching stopped at the InGaP layer, without etching the GaAs NWs. Since NWs in each pad had different diameters and periods, they absorb different wavelengths of light and have different colors in the light microscope images.

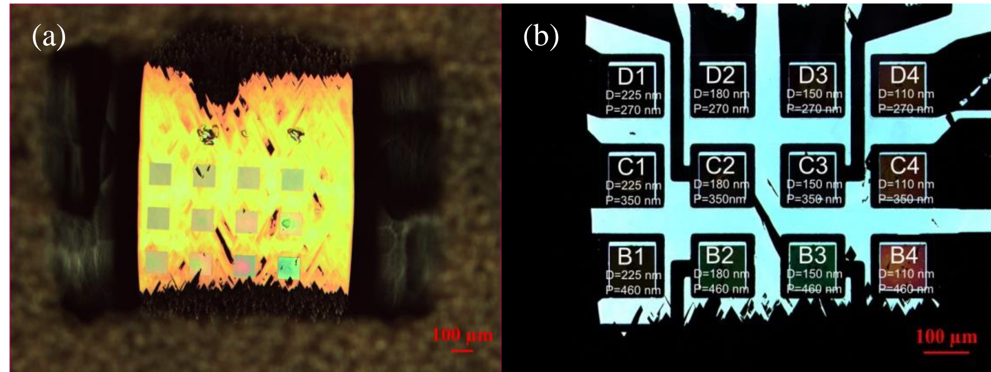

Figure 5.4. Light microscope images of NW pads after etching in a) reflection mode; and b) transmission mode.

5.2.2 Reflectance and Transmittance Measurement

Figure 5.5(a) shows the experimental setup of reflectance measurements of NW pads. The sample was mounted on a three-axis stage so that different pads could be selected for analysis. An Ocean Optics LS-1 light source with tungsten halogen lamp was used as the light source in this setup. The primary light beam passed a collimator (L5) to narrow the beam waist. The beam passed the beam splitter (BS1) and the objective lens L1 and was reflected by the NW pad before being collected by L2. After passing L2, the beam was split again by the second beam splitter (BS2). Then, one split beam was collected by objective lens L3, while the other beam was coupled into a multimode optical fiber and was analyzed by an Ocean Optics Jaz spectrometer. In this setup, NW pads on the sample could be seen through L3 and their positions could be aligned for

analysis. Since L3 and the spectrometer shared the same beam, the area being analyzed in the spectrometer was the same area seen from L3. After measuring the interested NW pads, the sample was replaced by a mirror and the spectrum obtained was used as a reference to normalize the sample reflectance spectrum. The setup used in transmittance measurements (**Figure 5.5(b)**) was very similar to the reflectance measurement setup. The only difference was that the light source was moved to the other side of the sample and lens L5 was removed. The area between the NW pads (off-pad area) was also analyzed to create a reference spectrum for normalization of the sample transmittance spectrum. The analyzed spot on each NW pad was circular and had a diameter of ~70 μm.

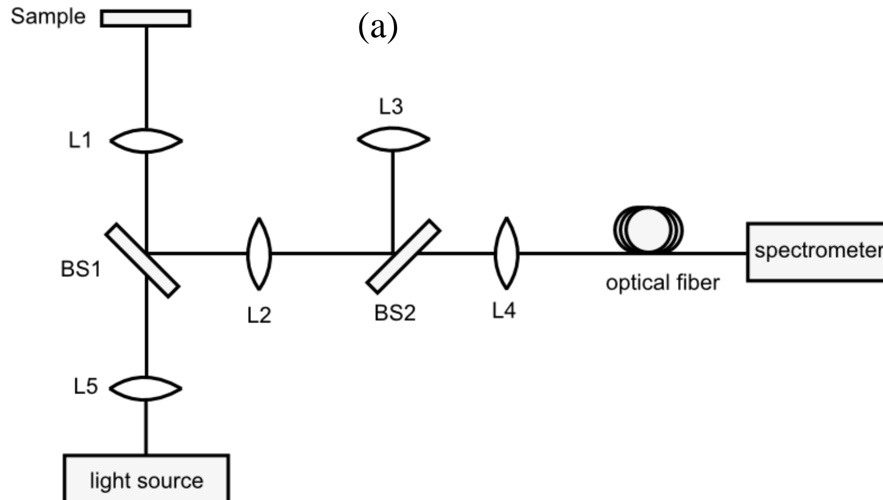

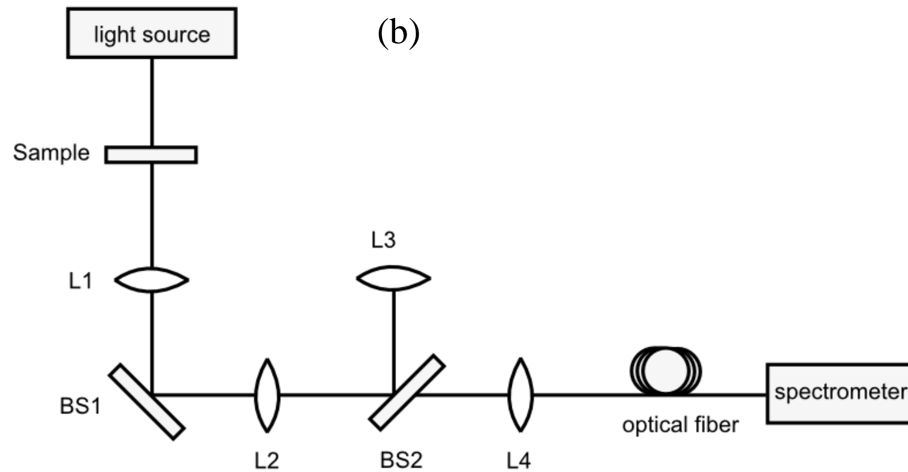

Figure 5.5. Experimental setup for (a) reflectance measurement; and (b) transmission measurement for NW pads.

5.3 Results and Discussion

Transmittance (T), reflectance (R) and absorptance (A) over a wavelength range of 400 nm to 1000 nm were used to evaluate optical properties of the NW pads. Transmittance of the NW arrays is plotted in **Figure 5.6**. In **Figure 5.6(a)**, each subplot shows NW arrays with the same P ((i): P=460 nm; (ii): P=350 nm; (iii): P=270 nm), but different D (D=110 nm; D=150 nm; D=180 nm; D=225 nm). By comparing curves in each subplot, the diameter dependence of each NW array transmittance can be seen. Decreasing D resulted in an increase in transmittance. For example, the transmittance of sample D2 was an average of 4.9 % over a wavelength range of 400 to 900 nm, while it was 8.1 % for D3. Decreasing D further to 110 nm, transmittance increased to 13.8% for

D4. **Figure 5.6(b)** compares transmittance of NW arrays with the same D ((i): D=110 nm; (ii): D=150 nm; (iii): D=180 nm; (iv): D=225 nm), but different P (P=460 nm; P=350 nm; P=270 nm) in each subplot. They showed the period dependence of NW array transmittance: decreasing P resulted in a decrease in transmittance. For instance, while decreasing P from 460 nm to 350 nm, transmittance decreased from 29.7% to 19.9% in the D=110 nm group. D4 had the lowest transmittance of 13.8%. As shown in **Figure 5.7**, the metal mask on the D1 array did not get lifted off, so D1 had a very low transmittance of 3.5%.

The peaks in the transmittance spectra matched the colors of NW arrays in the transmission light microscope images. In **Figure 5.6(a-i)**, transmittance curves of B2 and B3 had peaks around 550 nm (green light). This fact explained that B2 and B3 NW pads appeared green in the transmission light microscope image shown in **Figure 5.4(b)**. The same phenomenon could be seen in **Figure 5.6 (b-iv)**, where transmittance curves of B4, C4 and D4 pads had peaks around 700 nm (red light). Again, these peaks in the red color range were the reasons that B4, C4 and D4 pads appeared red in light microscope images (**Figure 5.4(b)**). While keeping NW diameter the same (D=100 nm) and decreasing NW periods from 460 nm (B4) to 350 nm (C4), and then to 270 nm (D4), NW pads appeared increasingly darker in light microscope images. D4 showed the darkest red among these three.

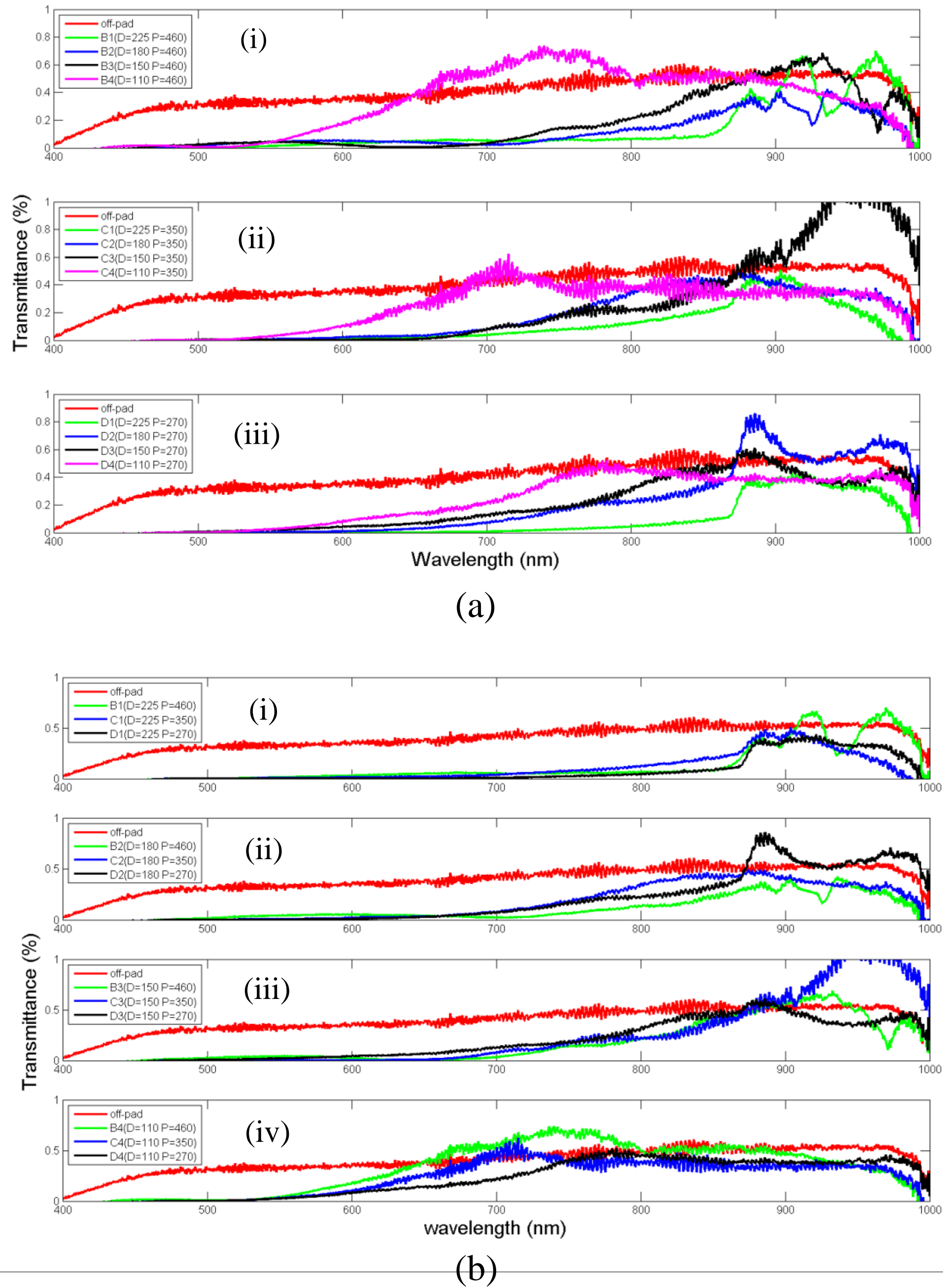

Figure 5.6. Transmittance of off-pad area and twelve nanowire arrays with various diameter D and period P. (a) Each subplot shows NW arrays with the same P ((i): P=460 nm; (ii): P=350 nm; (iii): P=270 nm), but different D (D=110 nm; D=150 nm; D=180 nm; D=225 nm); (b) Each subplot shows NW arrays with the same D((i): D=110 nm; (ii): D=150 nm; (iii): D=180 nm; (iv): D=225 nm), but different P (P=460 nm; P=350 nm; P=270 nm).

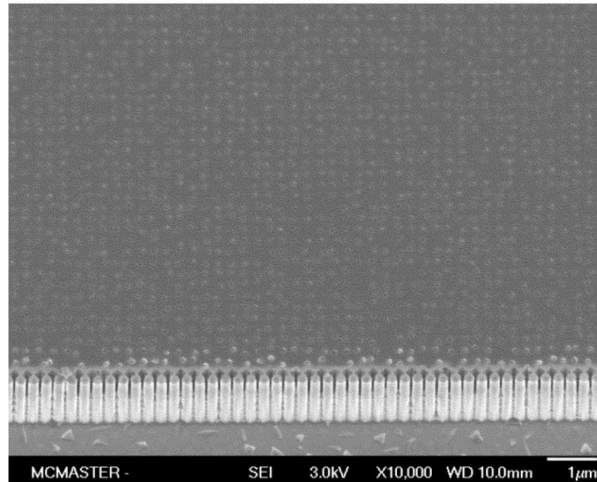

Figure 5.7. SEM image of as-etched NW array D1 showing that the metal mask did not get lifted-off.

Figure 5.8 shows the reflectance of NW arrays and the off-pad area. Since the InGaP film was not removed, reflectance in each measurement was generally higher than expected. The off-pad area showed a reflectance of 60.7%, and reflectance of all NW arrays was over 30%. To obtain accurate reflectance and D/P dependence of reflectance, the InGaP layer should be removed in further studies. Absorptance spectra of the NW arrays are shown in **Figure 5.9**, and the average absorptance from each NW array over a wavelength range of 400 nm to 900 nm is listed in **Table 5.2**. The off-pad area had the lowest absorptance of 5.8%, which would be contributed by the glass microslide, epoxy, cyclotene and InGaP film. Since D1 had residual metal film on top of the NW array, it showed the highest absorptance of 65.4%. Generally, a decrease in D while keeping P the same would result in a decrease in absorptance. Taking the P=350 nm group (C1, C2, C3 and C4) as an example, the absorptance dropped from 62.9% to 59.4% when D decreased from 225 nm to 180 nm. While D decreased further to 150 nm and 110 nm, the absorptance decreased to 58.4% and 37.2%, respectively. Due to the residual InGaP film,

the change in reflectance is minor. Thus, the increase in transmittance contributed to the decrease in absorptance more than the increase in reflectance did.

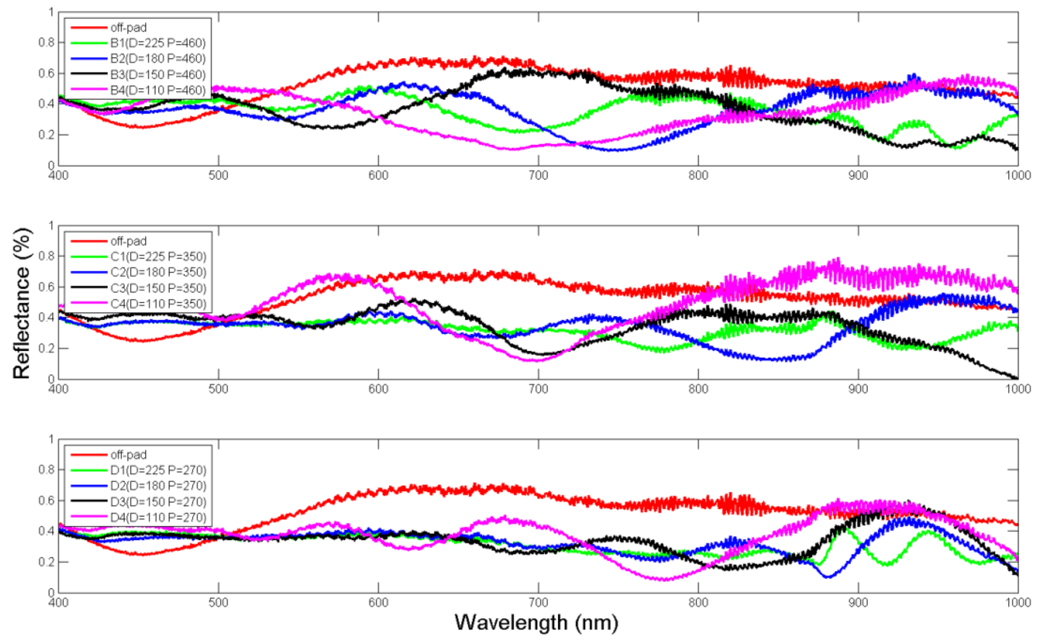

Figure 5.8. Reflectance of off-pad area and twelve nanowire arrays with various D and P. (a) Each subplot shows NW arrays with the same P ((i): P=460 nm; (ii): P=350 nm; (iii): P=270 nm), but different D (D=110 nm; D=150 nm; D=180 nm; D=225 nm).

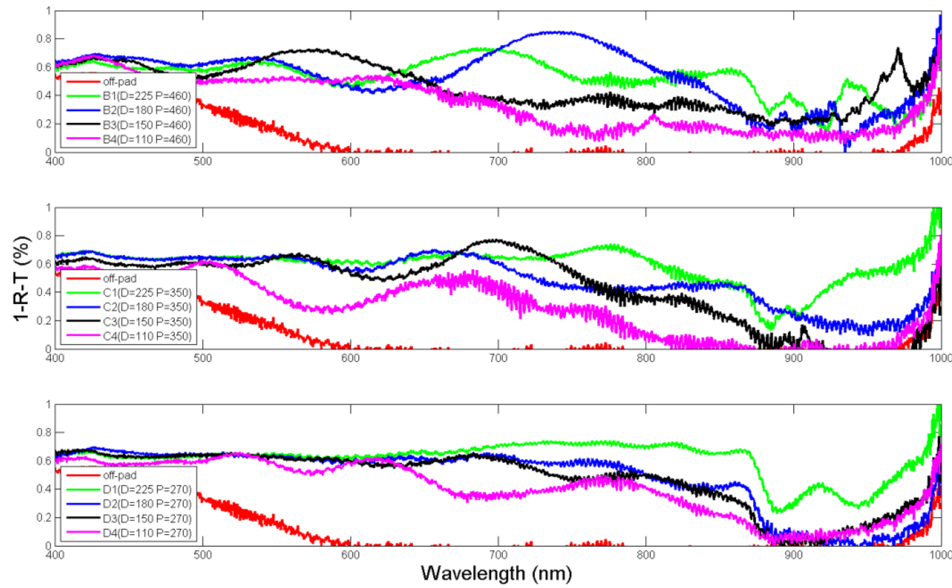

Figure 5.9. Absorptance (1-R-T) of off-pad area and twelve nanowire arrays with various D and P. (a) Each subplot shows NW arrays with the same P ((i): P=460 nm; (ii): P=350 nm; (iii): P=270 nm), but different D (D=110 nm; D=150 nm; D=180 nm; D=225 nm).

Table 5.2. Average absorptance of NW pads over 400 nm to 900 nm wavelength range.

	B1	**B2**	**B3**	**B4**
Absorptance	58.6%	58.2%	53.4%	42.2%
	C1	**C2**	**C3**	**C4**
Absorptance	62.9%	59.4%	58.4%	37.2%
	D1	**D2**	**D3**	**D4**
Absorptance	65.4%	60.2%	58.3%	49.6%
	Off-pad			
Absorptance	5.8%			

5.4 Conclusion

In this work, substrate-free GaAs NW arrays were successfully obtained by a combination of ICP-RIE and selective chemical etching. Optical characteristics of NW arrays with different NW diameters and periods were firstly measured experimentally. Although the residual InGaP film on the sample resulted in a high reflectance in the measurement, the D/P dependence of absorption could still be seen clearly. To obtain more accurate absorption results, the InGaP layer should be removed in future work.

6 Conclusions and Future Work

6.1 Thesis Summary

An ideal front contact for GaAs NW optoelectronic devices should meet three requirements: high transmittance, low sheet resistance and low contact resistance. ITO has low sheet resistance and high transmittance in the visible range, which makes it an ideal material for front contacts. However, performance degradation in GaAs NW devices have been reported due to poor performance of ITO contacts or other TCO contacts. To address this issue, an In/ITO contact with 13 Ω/□ sheet resistance, 89% transmittance and 0.13 $\Omega\cdot cm^2$ specific contact resistance to 8×10^{18} cm^{-3} doped n-type GaAs NWs was developed. In this work, gaps between NWs were filled with cyclotene to minimize contact pad sheet resistance and prevent shunts. Insertion of a thin indium layer between ITO and GaAs NWs followed by heat treatment created a graded InGaAs layer to lower the contact resistance.

Since the CTE of ITO is much lower than that of cyclotene, cracks were observed on ITO contacted samples. A contact crack test showed that the cracking issue was solved by inserting an indium layer between ITO and NWs. In In/ITO contacted samples, indium may have acted like a “lubricant” that prevented the expanding cyclotene from tearing the ITO apart. With regards to the concern that p-n junctions in NWs could be shorted due to indium diffusion, an indium diffusion test was done with FIB, TEM and

EDS to determine the significance of diffusion. EDS results showed that indium could not be found 177 nm below the contact/NW interface, which means p-n junctions below this depth would not be affected. In addition, the fact that In/ITO contacted planar solar cells had a higher efficiency than ITO contacted cells also proved that indium diffusion was not significant enough to affect p-n junctions. It was also evidence that In/ITO had a better contact performance than ITO.

Previous work has shown NW arrays have excellent light trapping effects, and absorption of NW arrays depends on the NW diameter-period (D-P) configuration. However, due to difficulties in obtaining high quality substrate-free NW arrays, absorption of NW arrays have not been measured experimentally until now. In this work, a technique combining ICP-RIE and selective chemical etching has been developed to obtain substrate-free NW arrays. Transmittance of NW arrays with various D-P configurations was determined experimentally for the first time. D/P dependence of NW array absorption has also been analyzed.

6.2 Future Work

While the In/ITO contact has achieved low contact resistance to n-GaAs NWs and it improved efficiency of planar GaAs solar cells, performance of In/ITO contact on p-GaAs NWs has not been characterized yet. Indium film thickness and annealing

temperature may be optimized to achieve a higher transmittance and a lower contact resistance. It would also be worthwhile to determine the performance of In/ITO contacts on other GaAs NW optoelectronic devices such as photodetectors and laser diodes. Although EDS showed the indium diffusion was not significant to destroy p-n junctions in NWs, the diffusion length of indium has not been specified accurately. SIMS has a lower detection limit than EDS and it can generate detailed depth profiles. Performing SIMS analysis on a sample both before and after annealing can not only determine the indium diffusion length, but also show the composition change of contact material during annealing.

The technique used in obtaining substrate-free NW arrays made it possible to measure transmittance of NW, which is a big step in optical characterization of NW arrays. However, improvements on this technique are strongly motivated. First of all, a more selective chemical solution would be helpful to ensure the InGaP layer is not etched. Secondly, while the remaining etch stop layer has significant effects on optical measurements, a technique needs to be developed to remove it without affecting NWs. Finally, future work on determining absorption of NWs made of different materials and different D-P configurations would also be valuable for future NW optoelectronic devices.

Reference

[1] H. Bi and R. R. Lapierre, Nanotechnology **20**, 465205 (2009).

[2] A. C. E. Chia and R. R. Lapierre, Nanotechnology **22**, 245304 (2011).

[3] M. C. Plante and R. R. LaPierre, J. Cryst. Growth **310**, 356 (2008).

[4] J. Zhang, a C. E. Chia, and R. R. LaPierre, Semicond. Sci. Technol. **29**, 054002 (2014).

[5] A. I. Persson, M. W. Larsson, S. Stenström, B. J. Ohlsson, L. Samuelson, and L. R. Wallenberg, Nat. Mater. **3**, 677 (2004).

[6] H. Yu and W. E. Buhro, Adv. Mater. **15**, 416 (2003).

[7] J. A. Czaban, D. A. Thompson, and R. R. LaPierre, Nano Lett. **9**, 148 (2009).

[8] R. R. LaPierre, J. Appl. Phys. **110**, 014310 (2011).

[9] R. R. LaPierre, A. C. E. Chia, S. J. Gibson, C. M. Haapamaki, J. Boulanger, R. Yee, P. Kuyanov, J. Zhang, N. Tajik, N. Jewell, and K. M. A. Rahman, Phys. Status Solidi - Rapid Res. Lett. **7**, 815 (2013).

[10] Y. Sun and J. a. Rogers, Nano Lett. **4**, 1953 (2004).

[11] K. Chen, J.-J. He, M.-Y. Li, and R. Lapierre, Chinese Phys. Lett. **29**, 036105 (2012).

[12] R. S. Wagner and W. C. Ellis, Appl. Phys. Lett. **4**, 89 (1964).

[13] P. Krogstrup, H. I. Jørgensen, M. Heiss, O. Demichel, J. V. Holm, M. Aagesen, J. Nygard, and A. Fontcuberta i Morral, Nat. Photonics **7**, 306 (2013).

[14] a C. E. Chia, J. P. Boulanger, and R. R. LaPierre, Nanotechnology **24**, 045701 (2013).

[15] L. Jalabert, P. Dubreuil, F. Carcenac, S. Pinaud, L. Salvagnac, H. Granier, and C. Fontaine, Microelectron. Eng. **85**, 1173 (2008).

[16] J.-J. Chao, D.-S. Wang, S.-C. Shiu, S.-C. Hung, and C.-F. Lin, Semicond. Sci. Technol. **25**, 065014 (2010).

[17] B. Hua, J. Motohisa, Y. Kobayashi, S. Hara, and T. Fukui, Nano Lett. **9**, 112 (2009).

[18] H. Wang, Appl. Phys. Lett. **103**, 093101 (2013).

[19] B. Ganjipour, J. Wallentin, M. T. Borgström, L. Samuelson, and C. Thelander, ACS Nano **6**, 3109 (2012).

[20] G. Mariani, R. B. Laghumavarapu, B. Tremolet de Villers, J. Shapiro, P. Senanayake, A. Lin, B. J. Schwartz, and D. L. Huffaker, Appl. Phys. Lett. **97**, 013107 (2010).

[21] G. Mariani, A. C. Scofield, C. Hung, and D. L. Huffaker, Nat. Commun. **4**, 1497 (2013).

[22] G. Mariani, P. Wong, A. M. Katzenmeyer, F. Léonard, J. Shapiro, and D. L. Huffaker, Nano Lett. **11**, 2490 (2011).

[23] N. Tajik, Z. Peng, P. Kuyanov, and R. R. LaPierre, Nanotechnology **22**, 225402 (2011).

[24] C. Colombo, M. Heiβ, M. Grätzel, and A. Fontcuberta i Morral, Appl. Phys. Lett. **94**, 173108 (2009).

[25] J.-J. Chao, S.-C. Shiu, and C.-F. Lin, Sol. Energy Mater. Sol. Cells **105**, 40 (2012).

[26] J. A. Czaban, D. A. Thompson, and R. R. LaPierre, Nano Lett. **9**, 148 (2009).

[27] G. E. Cirlin, A. D. Bouravleuv, I. P. Soshnikov, V. G. Dubrovskii, E. M. Arakcheeva, E. M. Tanklevskaya, and P. Werner, 360 (2010).

[28] N. Han, F. Wang, S. Yip, J. J. Hou, and F. Xiu, **013105**, 10 (2012).

[29] T. S. Kuan, P. E. Batson, T. N. Jackson, H. Rupprecht, and E. L. Wilkie, J. Appl. Phys. **54**, 6952 (1983).

[30] T. Margalith, O. Buchinsky, D. a. Cohen, a. C. Abare, M. Hansen, S. P. DenBaars, and L. a. Coldren, Appl. Phys. Lett. **74**, 3930 (1999).

[31] J. Wallentin, N. Anttu, D. Asoli, M. Huffman, I. Aberg, M. H. Magnusson, G. Siefer, P. Fuss-Kailuweit, F. Dimroth, B. Witzigmann, H. Q. Xu, L. Samuelson, K. Deppert, and M. T. Borgström, Science **339**, 1057 (2013).

[32] H. Goto, K. Nosaki, K. Tomioka, S. Hara, K. Hiruma, J. Motohisa, and T. Fukui, Appl. Phys. Express **2**, 035004 (2009).

[33] J. C. Shin, K. H. Kim, K. J. Yu, H. Hu, L. Yin, C. Ning, J. A. Rogers, J. Zuo, and X. Li, Nano Lett. **11**, 4831 (2011).

[34] Z. Gu, P. Prete, N. Lovergine, and B. Nabet, J. Appl. Phys. **109**, 064314 (2011).

[35] Y. Hu, M. Li, J.-J. He, and R. R. LaPierre, Nanotechnology **24**, 065402 (2013).

[36] M. Khorasaninejad, S. Patchett, J. Sun, and S. S. Saini, **024304**, (2013).

[37] V. L. Rideout, Solid. State. Electron. **18**, 541 (1975).

[38] A. G. Baca, F. Ren, J. . Zolper, R. . Briggs, and S. . Pearton, Thin Solid Films **308-309**, 599 (1997).

[39] T. Nittono, H. Ito, O. Nakajima, and T. Ishibashi, Jpn. J. Appl. Phys. **27**, 1718 (1988).

[40] A. A. Lakhani, J. Appl. Phys. **56**, 1888 (1984).

[41] M. Murakami, W. H. Price, Y. Shih, N. Braslau, K. D. Childs, and C. C. Parks, J. Appl. Phys. **62**, 3295 (1987).

[42] M. Murakami, Y. Shih, W. H. Price, E. L. Wilkie, K. D. Childs, and C. C. Parks, J. Appl. Phys. **64**, 1974 (1988).

[43] J. R. Bosnell and R. Waghorne, Thin Solid Films **15**, 141 (1973).

[44] J. C. C. Fan and J. B. Goodenough, J. Appl. Phys. **48**, 3524 (1977).

[45] H. Kim, C. M. Gilmore, A. Piqué, J. S. Horwitz, H. Mattoussi, H. Murata, Z. H. Kafafi, and D. B. Chrisey, J. Appl. Phys. **86**, 6451 (1999).

[46] Y. Zhong, Y. C. Shin, C. M. Kim, B. G. Lee, E. H. Kim, Y. J. Park, K. M. A. Sobahan, C. K. Hwangbo, Y. P. Lee, and T. G. Kim, J. Mater. Res. **23**, 2500 (2008).

[47] R. Bel Hadj Tahar, T. Ban, Y. Ohya, and Y. Takahashi, J. Appl. Phys. **83**, 2631 (1998).

[48] J. Bae, H. Kim, X.-M. Zhang, C. H. Dang, Y. Zhang, Y. J. Choi, A. Nurmikko, and Z. L. Wang, Nanotechnology **21**, 095502 (2010).

[49] C. Hsu, S. Chang, Y.-R. Lin, P. Li, T. Lin, S. Tsai, T. Lu, and I. Chen, Chem. Phys. Lett. **416**, 75 (2005).

[50] J. Wallentin, N. Anttu, D. Asoli, M. Huffman, I. Aberg, M. H. Magnusson, G. Siefer, P. Fuss-Kailuweit, F. Dimroth, B. Witzigmann, H. Q. Xu, L. Samuelson, K. Deppert, and M. T. Borgström, Science **339**, 1057 (2013).

[51] K. Sreenivas, T. Sudersena Rao, A. Mansingh, and S. Chandra, J. Appl. Phys. **57**, 384 (1985).

[52] J. Szczyrbowski, A. Dietrich, and H. Hoffmann, Phys. Status Solidi **78**, 243 (1983).

[53] M. Higuchi, S. Uekusa, R. Nakano, and K. Yokogawa, J. Appl. Phys. **74**, 6710 (1993).

[54] J. Bregman, Y. Shapira, and H. Aharoni, J. Appl. Phys. **67**, 3750 (1990).

[55] B. Bessais, N. Mliki, and R. Bennaceur, Semicond. Sci. Technol. **8**, 116 (1993).

[56] N. Balasubramanian and A. Subrahmanyam, Mater. Sci. Eng. B **1**, 279 (1988).

[57] H. Haitjema and J. J. P. Elich, Thin Solid Films **205**, 93 (1991).

[58] P. Williams, Ann. Rev. Mater. Sci. **15**, 517 (1985).

[59] D. K. Schroder, *MATERIAL AND DEVICE SEMICONDUCTOR MATERIAL AND DEVICE Third Edition*, 3rd ed. (John Wiley & Sons, Inc.,Hoboken, New Jersey, 2006).

[60] B. Hagenhoff, Mikrochim. Acta **271**, 259 (2000).

[61] R. A. Bruce and G. R. Piercy, Solid. State. Electron. **30**, 729 (1987).

[62] G. Stareev, Appl. Phys. Lett. **62**, 2801 (1993).

[63] J. Wallentin, N. Anttu, D. Asoli, M. Huffman, I. Aberg, M. H. Magnusson, G. Siefer, P. Fuss-Kailuweit, F. Dimroth, B. Witzigmann, H. Q. Xu, L. Samuelson, K. Deppert, and M. T. Borgström, Science **339**, 1057 (2013).

[64] R. J. Yee, S. J. Gibson, V. G. Dubrovskii, and R. R. LaPierre, Appl. Phys. Lett. **101**, 263106 (2012).

[65] A. C. E. Chia and R. R. LaPierre, Nanotechnology **22**, 245304 (2011).

[66] a C. E. Chia, M. Tirado, F. Thouin, R. Leonelli, D. Comedi, and R. R. LaPierre, Semicond. Sci. Technol. **28**, 105026 (2013).

[67] Http://www.dow.com (2012).

[68] J. Lin, F. Su, C. Chien, T. Su, W. Lin, Y. Jhuang, J. Che, and J. Li, *Imaging Methods for Novel Materials and Challenging Applications, Volume 3* (Springer New York, New York, NY, 2013), pp. 353–358.

[69] E. V Vernon and S. Weintroub, Proc. Phys. Soc. Sect. B **66**, 887 (1953).

[70] M. Khorasaninejad, N. Abedzadeh, A. Singh Jawanda, N. O, M. P. Anantram, and S. Singh Saini, J. Appl. Phys. **111**, 044328 (2012).

[71] Http://www.eag.com, (2014).

[72] L. Wen, Z. Zhao, X. Li, Y. Shen, H. Guo, and Y. Wang, Appl. Phys. Lett. **99**, 143116 (2011).

[73] S. Link, M. B. Mohamed, and M. a. El-Sayed, J. Phys. Chem. B **103**, 3073 (1999).

[74] V. Sivakov, G. Andrä, A. Gawlik, A. Berger, J. Plentz, F. Falk, and S. H. Christiansen, Nano Lett. **9**, 1549 (2009).

[75] a J. Standing, S. Assali, J. E. M. Haverkort, and E. P. a M. Bakkers, Nanotechnology **23**, 495305 (2012).

[76] J. Yang, Z. Peng, D. Cheong, and R. Kleiman, IEEE J. Photovoltaics 1 (2014).

[77] W. S. Hobson, Y. K. Chen, and M. C. Wu, Semicond. Sci. Technol. **7**, 1425 (1992).